AN INVESTIGATION OF THE EFFECTS OF HUMAN DYNAMICS ON SYSTEM STABILITY AND PERFORMANCE

A THESIS SUBMITTED TO
THE GRADUATE SCHOOL OF ENGINEERING AND SCIENCE
OF BILKENT UNIVERSITY
IN PARTIAL FULFILLMENT OF THE REQUIREMENTS FOR
THE DEGREE OF
MASTER OF SCIENCE
IN
MECHANICAL ENGINEERING

By
Ehsan Yousefi
August 2018

An Investigation of the Effects of Human Dynamics on System Stability and Performance
By Ehsan Yousefi
August 2018

We certify that we have read this thesis and that in our opinion it is fully adequate, in scope and in quality, as a thesis for the degree of Master of Science.

Yıldıray Yıldız(Advisor)

Onur Özcan

Özgür Ünver

Approved for the Graduate School of Engineering and Science:

Ezhan Karaşan
Director of the Graduate School

ABSTRACT

AN INVESTIGATION OF THE EFFECTS OF HUMAN DYNAMICS ON SYSTEM STABILITY AND PERFORMANCE

Ehsan Yousefi
M.S. in Mechanical Engineering
Advisor: Yıldıray Yıldız
August 2018

Considered as a challenging element of closed-loop structures, the human operator, and his/her interactions with the underlying system, should be carefully analyzed to obtain a safe and high performing system. In this thesis, the interaction between human dynamics and the closed loop system is investigated for two different scenarios. The first scenario consists of a flight control system controlled by an adaptive controller. A telerobotic system where the controllers are conventional linear controllers is analyzed in the second scenario. Although model reference adaptive control (MRAC) offers mathematical design tools to effectively cope with many challenges of the real world control problems such as exogenous disturbances, system uncertainties, and degraded modes of operations, when faced with human-in-the-loop settings, these controllers can lead to unstable system trajectories in certain applications. To establish an understanding of stability limitations of MRAC architectures in the presence of humans, a mathematical framework is developed for the first scenario, whereby an MRAC is designed in conjunction with a class of linear human models including human reaction delays. This framework is then used to reveal, through stability analysis tools, the stability limit of the MRAC-human closed loop system and the range of model parameters respecting this limit. An illustrative numerical example of an adaptive flight control application with a Neal-Smith pilot model is utilized to demonstrate the effectiveness of the developed approaches. The effect of a linear filter, inserted between the human model and MRAC, on the closed loop stability is also investigated. Related to this, a mathematical approach to study how the error dynamics of MRAC could favorably or unfavorably influence human operator's error dynamics in performing a certain task is analyzed. An illustrative numerical example concludes the study. For the second scenario, stability properties of three different human-in-the-loop telerobotic system architectures are comparatively investigated, in the presence of human reaction time-delay and communication time-delays. The challenging problem of stability characterization of systems with multiple time-delays is addressed by implementing rigorous stability analysis tools, and the results are verified via numerical illustrations. Practical insights about the results of the stability investigations are also provided. Finally, apart from these scenarios, after the observation that a simple linear transfer function model for a real force reflecting haptic device, which is used in telerobotics applications, is missing, a data-driven and first principles modeling of the Geomagic$^{\circledR}$ Touch$^{\text{TM}}$ (formerly PHANToM$^{\circledR}$ Omni$^{\circledR}$) haptic device is considered. A simple linear model is provided for one of the degrees of freedom based on fundamental insights into the device structure and in light of experimental observations.

Keywords: Human-in-the-Loop Systems, Model Reference Adaptive Control, Closed-Loop System Stability, Telerobotics, Time-Delay Systems, Modelling, PHANToM$^{\circledR}$ Omni$^{\circledR}$.

ÖZET

İNSAN DİNAMİĞİNİN SİSTEM KARARLILIĞI VE PERFORMANSINA ETKİLERİNİN İNCELENMESİ

Ehsan Yousefi
Makine Mühendisliği, Yüksek Lisans
Tez Danışmanı: Yıldıray Yıldız
Ağustos 2018

Kapalı devre yapıların zorlayıcı bir unsuru olarak düşünülen insan dinamikleri ve bu dinamiklerin sistemle olan etkileşimleri, güvenli ve yüksek performanslı bir sistem elde etmek için dikkatlice analiz edilmelidir. Bu tezde, insan dinamikleri ile kapalı döngü kontrol sistemi arasındaki etkileşim iki farklı senaryo için incelenmiştir. İlk senaryo, uyarlamalı kontrolör tarafından kontrol edilen bir uçuş kontrol sisteminden oluşmuştur. İkinci senaryoda ise, konvansiyonel doğrusal kontrolcüler tarafından kontrol edilen bir telerobotik sistem analiz edilmiştir. Her ne kadar model referans uyarlamalı kontrol (MRAC) dış bozucu etkiler, sistem belirsizlikleri ve bozulmuş operasyon modları gibi gerçek kontrol problemlerinin birçok zorluğu ile etkili bir şekilde başa çıkabilmek için matematiksel tasarım araçları sunsa da, insanın döngü içinde olduğu sistemlerde, bu kontrolcüler kararsız sistem yörüngelerine yol açabilir. Bu sebeple, insanın döngü içinde etkin olduğu sistemlerde, MRAC mimarilerinin kararlılık limitleri hakkında bir kavrayış geliştirebilmek için, ilk senaryoda MRAC ve tepki gecikmesine sahip bir insan modelinden oluşan bir sistem oluşturulmuştur. Daha sonra bu yapı, kararlılık analiz araçları kullanılarak incelenmiş ve sistem parametrelerinin kararlılık sınırları içinde kalan aralıkları tespit edilmiştir. Geliştirilen yaklaşımların etkinliğini göstermek için bir Neal-Smith pilot modeli ile uyarlamalı bir uçuş kontrol sisteminden oluşan bir numerik benzetim örneği kullanılmıştır. İnsan modeli ile MRAC arasına yerleştirilen doğrusal bir filtrenin, kapalı döngü kararlılığı üzerindeki etkisi de araştırılmıştır. Bununla ilgili olarak, MRAC'ın hata dinamiğinin, belirli bir görevi yerine getirirken insan operatörünün hata dinamiklerini olumlu veya olumsuz yönde nasıl etkilediği incelenmiş ve numerik bir örnek verilmiştir. İkinci senaryo için, üç farklı insanın-döngü-içinde-olduğu telerobotik sistem mimarisinin kararlılık özellikleri, insan tepkisi zaman gecikmesi ve iletişim zaman gecikmelerinin mevcudiyetinde karşılaştırmalı olarak araştırılmıştır. Çoklu zaman gecikmeli sistemlerin kararlılık karakteristiklerinin çıkarılması problemi, titiz kararlılık analiz araçlarının uygulanmasıyla ele alınmış, sonuçlar nümerik benzetimlerle doğrulanmış, ve bu kararlılık araştırmalarının pratik sonuçları da verilmiştir. Son olarak, bu senaryoların yanı sıra, telerobotik uygulamalarında kullanılan Geomagic$^{\circledR}$ Touch$^{\text{TM}}$ (eskiden, PHANToM$^{\circledR}$ Omni$^{\circledR}$) haptik cihazının modellenmesi problemi ele alınmıştır. Cihazın yapısı ve deneysel gözlemler ışığında temel prensiplere dayanan doğrusal bir model, serbestlik derecelerinden birisi için geliştirilmiştir.

Anahtar sözcükler: Döngü İçinde İnsan Sistemleri, Model Referans Uyarlamalı Kontrol, Kapalı-döngü Sistem Kararlılığı, Telerobotik, Zaman Gecikmeli Sistemler, Modelleme, PHANToM$^{\circledR}$ Omni$^{\circledR}$.

Acknowledgement

I would like to express my sincere gratitude to my advisor, Assistant Professor Dr. Yıldıray Yıldız, for his kind supervision, patience, encouragement, comprehensive advices, and more importantly, for what I learned beyond the academics, the life lessons, and professional attitude which for sure will be with me throughout my entire life. I would like to thank Associate Professor Dr. Rıfat Sipahi and Assistant Professor Dr. Tansel Yucelen for their constant guidance and considerations. It is my duty to appreciate Assistant Professor Dr. Onur Özcan's advices throughout my research work and education, especially with the laboratory facilities. I would like to thank Dr. Şakir Baytaroğlu for his time and consideration with utilizing the laboratory tools and facilities.

No success can be accomplished without the support of the great, my kind family, who has always been with me, though from hundreds of kilometers away. There is no distance when the hearts are bound and the love is devoted.

It is my pleasure to have the company of the kind, my friends and colleagues. I would like to thank all of them for the all unforgettable memories that they have created for me beyond reckoning. You will stay in my heart forever and I would like to remember you by my heart and not by falling to the cliché of listing the names.

My heart goes out to a very lovable member of our family, my grandmother, whom I lost during my thesis work and even could not say the last goodbye to her. May she rest in peace.

Last but not least, this work is dedicated to the all broken souls never surrender, whatever the cost and the agony may be.

Contents

List of Figures

List of Tables

Chapter 1

Introduction

Human operator as an element of the overall system plays a crucial role in closed loop settings [1], where she/he is in control of a system with which she/he is exchanging information in various forms whether visual or haptic. In this thesis, stability and performance of two human-in-the-loop systems, an adaptive control system and a telerobotic system are investigated. Each of these systems should be analyzed separately due to the inherent subtleties of each structure, which, in turn, reflects the fundamental challenges in analyzing human-in-the-loop dynamics in a mathematically rigorous manner. In terms of mathematical modeling of human behavior, many studies focus on developing a representative transfer function of the human in a specific task within a certain frequency band. Three key models, *i)* human driver models [2], *ii)* McRuer crossover model [3], and *iii)* Neal-Smith pilot model [4–8] can be given as examples for these models. Human driver models are proposed in the context of car driving, specifically in longitudinal car-following tasks in a fixed lane. While these models vary depending on the degree of their complexity (see [9]), their simplest form is a pure time delay representing the dead time between arrival of stimulus and reaction produced by the driver. McRuer's model, on the other hand, is proposed to capture human pilot behavior, to further understand flight stability and human-vehicle integration. Among many of its variations, this model is essentially an integrator dynamics with a time lag to capture human reaction delays and a gain modulated to maintain a specific bandwidth. Similarly, the Neal-Smith pilot model, which is essentially a first order lead-lag type compensator with a gain and time lag, can be utilized to study the behavior of human pilots [4–8].

Achieving stability and desired performance are the major challenges in control theory when dealing with uncertain dynamical systems. While fixed-gain robust control design approaches [10–13] can deal with such dynamical systems, the knowledge of system uncertainty bounds is required and characterization of these bounds is not trivial in general due to practical constraints such as extensive and costly verification and validation procedures. Furthermore, robust control approaches generally provide conservative control inputs. On the other hand, adaptive control design approaches [14–17] can effectively cope with the effects of system uncertainties and require less modeling work while providing "need based" control effort [18,19]. One of the well-known and important class of adaptive controllers is called a model reference adaptive controller (MRAC) [20,21], where the architecture includes a reference model, a parameter adjustment mechanism, and a controller. In this setting, a desired closed-loop dynamical system behavior is captured by the reference model, where its output (respectively, state) is compared with the output (respectively, state) of the uncertain dynamical system. This comparison yields a system error signal, which is used to drive an online parameter adjustment mechanism. Then, the controller adapts feedback gains to minimize this error signal using the information received from the parameter adjustment mechanism. As a consequence, under proper settings, the output of the uncertain dynamical system converges to the output of the reference model asymptotically in a stable manner.

While MRAC offers mathematical design tools to effectively cope with system uncertainties, the capabilities of MRAC when interfaced with human operators can be limited. Indeed, in certain applications when humans are in the loop [6, 8, 22, 23], the closed loop system with MRAC can become unstable. As a matter of fact, such problems are not only limited to MRAC-human interactions and have been reported to arise in various human-in-the-loop control problems including, for example, pilot-induced oscillations [24, 25]. To address these issues, novel control design ideas are proposed and experimentally tested including adaptive control as well as smart-cue/smart-gain concepts [24, 26]. On the other hand, an analytical framework aimed at understanding these phenomena and that can ultimately be used to drive rigorous control laws is currently lacking. These observations motivate this thesis where the main objective is to develop comprehensive models from a system-level perspective and analyze such models to develop a strong understanding of the aforementioned stability limits. The first scenario used in this thesis for this purpose is analyzed within the framework of human-in-the-loop MRAC architectures.

One critical parameter added to the control problem that can be responsible for instabilities of the human-in-the-loop systems is the human reaction delay — a topic which has long been investigated in the literature [2, 9, 27–29], but not treated in the context of human-in-the-loop adaptive control. It is known that the presence of time delays is a source of instability, which must be carefully dealt with and explicitly addressed in any control design framework [30, 31]. Delay-induced instability phenomenon has been recognized in numerous applications including robotics, physics, cyber-physical systems, and operational psychology [32]. For example, in physics literature, effects of human decision making process and reaction delays are studied to understand the arising car driving patterns, traffic flow characteristics, traffic jams, and stop-and-go waves [2, 33]. Therefore, it is of strong interest to understand the limitations of MRAC when coupled with human operators in a closed-loop setting. For this purpose, in this thesis, MRAC is first incorporated into a general linear human model with reaction delays. Through the use of Lyapunov stability theory, this model is then studied to reveal its fundamental stability limit, and the parameter space of the model where such limit is respected, producing stable trajectories. An illustrative numerical example of an adaptive flight control application with a Neal-Smith pilot model is utilized to demonstrate the effectiveness of the developed approaches. The main contribution of this part of the study is the development of a comprehensive control-theoretic modeling approach, where the dynamic interactions between a class of human models and MRAC framework can be investigated. Understanding how an ideal MRAC would perform in conjunction with a human model including human reaction delays and how such delays could pose strong limitations to the stabilization and performance of the closed-loop human-MRAC architecture is the main focus of this part of the study.

Delay-induced instability is a major problem in human-in-the-loop systems, and it is of strong interest to address this problem within the MRAC framework. In this thesis, it is proposed to insert a linear filter in between the human model and MRAC, to be designed strategically with the aim to enhance both stability and performance characteristics of the combined MRAC-human-filter closed-loop dynamics. Moreover, the coupling between MRAC and the human model creates an interesting coupling, which must be carefully studied for the overall synergistic collaboration between MRAC and the human. Therefore, the effects of a linear filter on stability limits of human-in-the-loop MRAC systems is also investigated in this study. It is found that the proposed filter can effectively increase stability limits of the overall closed-loop system. Moreover, the effect of the error dynamics of MRAC on the error dynamics arising in the response of human while trying to achieve a certain task (for example, step input tracking) is investigated. The result of this study shows that the proposed filter can also be useful in reducing the critical frequency of the error dynamics (that the human operator sees and acts based upon) up to an order of magnitude less than its original value.

Teleoperation is an enabler of interaction between a local operator and a distant environment, and therefore, another venue where humans interact with closed loop control systems. Application areas of this technology includes underwater operations, space explorations, telediagnosis and telesurgery, and even education [34,35]. While relaying human operator's orders from the local side (master side) to the remote side (slave side), a teleoperation system can provide the operator with a feeling of the remote environment with visual, auditory, and haptic signals that are fed back from the remote site [36]. This architecture, in which there is a two way communication between the master and the slave sides, is called a bilateral teleoperation system. The purpose of the study conducted in this thesis about teleoperation is to comparatively analyze the stability characteristics of three different human-in-the loop telerobotic schemes with different remote signal feedback structures, in the presence of human operator and communication time-delays.

It is well-known that time-delays could result in system instability, and also degrade operator's performance, hence can jeopardize the purpose of teleoperation as a human-in-the-loop system [37–39]. Other examples of detriments of time-delays, including undesired oscillations and limited parameter space of stable operation, are discussed in [32].

Human as an element of the telerobotic system has been investigated in the literature. In [40], authors incorporated the minimum jerk model [41] to predict the future inputs of the human operator. They experimentally showed that the system has improved performance when this prediction is used in the controller development. In [42], authors conducted an experimental study in which they considered a linear model for the human operator, and showed its effectiveness in both stability and performance of the system. However, in their analysis, they did not consider the human operator reaction time-delay. In [43], authors considered a model of human operator in stability analysis and their PD-like controller design, where human reaction time-delay is considered. Indeed, it is well known in other research domains that human operator reaction time-delays play a crucial role in closed loop settings, e.g., car driving [44] and pilot induced oscillations [45–47].

From an architectural point of view, a bilateral telerobotic system can be categorized based on the transmitted signals between the master and slave systems. Position-position [48] and position-force [49] architectures are the very fundamental ones, and more complex multichannel architectures are also used for obtaining higher transparency and performance [34, 50]. Needless to say, the selection of the architecture is critical as it will affect the closed-loop dynamics and how well the human operator will utilize the teleoperation system to perform tasks.

In the second part of this thesis, human models with reaction time-delay (τ_h) are considered as an element of a teleoperation system with inherent communication time-delays (τ_c). The main objective of this study is to investigate the stability of the human-in-the-loop system with respect to these delays. Needless to say, this characterization can be quite difficult since the corresponding eigenvalue problem becomes challenging to handle due to time-delays [1, 32]. We rigorously compare the stability and performance of the telerobotic system at hand using [51,52], for three different practically-important configurations which differ from each other based on the communicated signals and controller usage. Specifically, the point of interest is understanding how communication and human reaction time-delays affect closed-loop stability properties. To this end, two different human-in-the-loop architectures are investigated, namely configurations 1 and 2, each with two independent time-delays, and compare their stability and performance characteristics with those of the baseline.

The final part of this thesis is related to modeling of a haptic device which is frequently used in telerobotics applications. The PHANToM®, which is a 3-dimensional (3D) force-reflecting haptic device, was originally designed by Massie and Salisbury [53] and commercialized by SensAble Technologies, Inc. and later by Geomagic®, Inc. Although PHANToM® Omni®, one of the most cost-effective haptic devices, has been widely used in the haptics and teleoperations fields for research and education purposes [54–58], a simple and easy-to-use linear mathematical model of this device has not been made publicly available, to the best of the author's knowledge. This model, especially in the pitch axis, can be difficult to obtain due to nonlinearities originating from the gravitational effects on the rotating arm whose dynamics is inherently unstable.

Authors of [59] and [60] studied the mechanical and electrical properties of PHANToM® model 1.5, and were able to provide a transfer function model. However, this model has different technical properties than PHANToM® Omni® (or Geomagic® Touch™) device. In [61], a second-order linear model of PHANToM® Omni® with varying coefficients was developed using the general form of dynamic analysis of robots and manipulators. As noted in [61], the resulting model complexity was a serious issue for controller development. In [62], the authors provided forward and inverse kinematic models of position and velocity of the PHANToM® Omni® device. They, therefore, could also provide kinesthetic force feedback model, i.e., the generalized torque needed to be exerted at each joint to provide a haptic sense of a virtual object. While the above mentioned studies successfully provided useful models, currently an experimentally validated model of the device, especially for the pitch axis, that can be used for controller design and closed loop system analysis is not available.

To address the above need, in this thesis, a linear model for PHANToM® Omni® is provided, which is simple enough to be employed for controller design. This model is focused on the pitch axis motion which is harder to model due to nonlinear gravitational effects and inherently unstable behavior. Both the physical device structure and experimental data are utilized to build a satisfactory model. Another experimentally verified modeling study can be found in [63], where an energy based system identification methodology was given. In [63], the nonlinear inertia, damping and the actuator gains were also identified. There are two main differences between this work and [63]. First, a minimal second-order state space differential equation model for the system is not assumed in this study. This assumption results in a model with time varying coefficients, which in turn could complicate controller design and implementation. Second, unlike [63], where the motion about the yaw axis is modeled, the motion about the pitch axis is modeled. It is noted that the motion about the pitch axis which experiences nonlinear gravitational effects while the motion in the yaw axis is not effected by these nonlinear forces.

This thesis includes four chapters. In Chapter 2, the human-MRAC interactions problem is investigated. In Chapter 3, human-control system interactions are analyzed in the domain of telerobotics. Chapter 4 is dedicated to the modeling of the PHANToM® Omni® device. Finally, Chapter 5 concludes the work by providing a summary of the discussions and the future directions.

Chapter 2

An Analysis of Stability and Performance in Human-in-the-Loop Model Reference Adaptive Control Architectures

Although model reference adaptive controllers offer mathematical tools to effectively cope with system uncertainties arising from idealized assumptions, linearization, model order reduction, exogenous disturbances, and degraded modes of operations, they can lead to unstable system trajectories in certain applications when humans are in the loop. In this chapter, stability of human-in-the-loop model reference adaptive control architectures is analyzed. For a general class of linear human models with time-delay, a fundamental stability limit of these architectures is established, which depends on the parameters of this human model as well as the reference model parameters of the adaptive controller. It is shown that when the given set of human model and reference model parameters satisfy this stability limit, the closed-loop system trajectories are guaranteed to be stable. Improving the stability and performance of this structure is then realized by

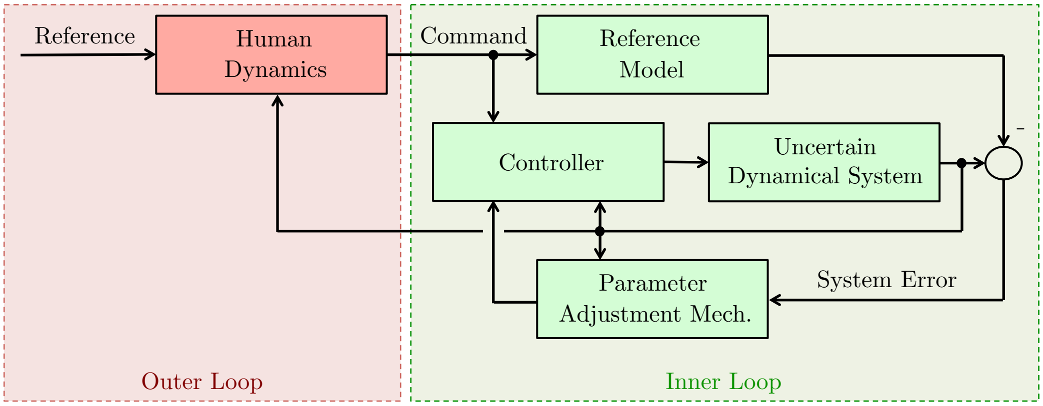

Figure 2.1: Block diagram of the human-in-the-loop model reference adaptive control architecture.

inserting a linear filter between the human operator and MRAC.

The notation used in this work is standard. Specifically, $\mathbb{R}$ denotes the set of real numbers, $\mathbb{R}^n$ denotes the set of $n \times 1$ real column vectors, $\mathbb{R}^{n\times m}$ denotes the set of $n \times m$ real matrices, $\mathbb{R}_+$ (resp., $\overline{\mathbb{R}}_+$) denotes the set of positive (resp., nonnegative-definite) real numbers, $\mathbb{R}_+^{n\times n}$ (resp., $\overline{\mathbb{R}}_+^{n\times n}$) denotes the set of $n \times n$ positive-definite (resp., nonnegative-definite) real matrices, $\mathbb{S}^{n\times n}$ denotes the set of $n \times n$ symmetric real matrices, $\mathbb{D}^{n\times n}$ denotes the $n \times n$ real matrices with diagonal scalar entries, $(\cdot)^T$ denotes transpose, $(\cdot)^{-1}$ denotes inverse, and "$\triangleq$" denotes equality by definition. In addition, we write $\lambda_{min}(A)$ (resp., $\lambda_{max}(A)$) for the minimum (resp., maximum) eigenvalue of the Hermitian matrix A, $tr(\cdot)$ for the trace operator, $vec(\cdot)$ for the column stacking operator, $||\cdot||_2$ for the Euclidian norm, $||\cdot||_\infty$ for the infinity norm, and $||\cdot||_F$ for the Frobenius matrix norm.

2.1 Problem Formulation

In order to study human-in-the-loop model reference adaptive controllers, the block diagram configuration is given in Figure 2.1. In the figure, the outer loop architecture includes the reference that is fed into the human dynamics to generate a command for the inner loop architecture in response to the variations resulting from the uncertain dynamical system. In this setting the, the reference input is what the human aims to achieve in a task, and the uncertain dynamical system is the machine on which this task is being performed. The inner loop architecture includes the uncertain dynamical system as well as the model reference adaptive controller components (i.e., the reference model, the parameter adjustment mechanism, and the controller). Specifically, at the outer loop architecture, a general class of linear human models with constant time-delay is considered given by

$$\begin{aligned} \dot{\xi}(t) &= A_h\xi(t) + B_h\theta(t-\tau), \quad \xi(0) = \xi_0, && (2.1) \\ c(t) &= C_h\xi(t) + D_h\theta(t-\tau), && (2.2) \end{aligned}$$

where $\xi(t) \in \mathbb{R}^{n_\xi}$ is the internal human state vector, $\tau \in \mathbb{R}_+$ is the internal human time-delay, $A_h \in \mathbb{R}^{n_\xi \times n_\xi}$, $B_h \in \mathbb{R}^{n_\xi \times n_r}$, $C_h \in \mathbb{R}^{n_c \times n_\xi}$, $D_h \in \mathbb{R}^{n_c \times n_r}$, and $c(t) \in \mathbb{R}^{n_c}$ is the command produced by the human, which is the input to the inner loop architecture as shown in Figure 2.1. Here, input to the human dynamics is given by

$$\theta(t) \triangleq r(t) - E_h x(t), \qquad (2.3)$$

where $\theta(t) \in \mathbb{R}^{n_r}$, with $r(t) \in \mathbb{R}^{n_r}$ being the bounded reference. Here $x(t) \in \mathbb{R}^n$ is the state vector (further details below) and $E_h \in \mathbb{R}^{n_r \times n}$ selects the appropriate states to be compared with $r(t)$. Note that the dynamics given by (2.1), (2.2), and (2.3) is general enough to capture, for example, widely studied linear time-invariant human models with time-delay including Neal-Smith model and its extensions [4–8].

Next, at the inner loop architecture, the considered uncertain dynamical system is given by

$$\dot{x}_p(t) = A_p x_p(t) + B_p \Lambda u(t) + B_p \delta_p(x_p(t)), \quad x_p(0) = x_{p_0}, \qquad (2.4)$$

where $x_p(t) \in \mathbb{R}^{n_p}$ is the accessible state vector, $u(t) \in \mathbb{R}^m$ is the control input, $\delta_p : \mathbb{R}^{n_p} \to \mathbb{R}^m$ is an uncertainty, $A_p \in \mathbb{R}^{n_p \times n_p}$ is a known system matrix, $B_p \in \mathbb{R}^{n_p \times m}$ is a known control input matrix, and $\Lambda \in \mathbb{R}_+^{m \times m} \cap \mathbb{D}^{m \times m}$ is an unknown control effectiveness matrix. Furthermore, it is assumed that the pair (A_p, B_p) is controllable and the uncertainty is parameterized as

$$\delta_p(x_p) \;=\; W_p^T \sigma_p(x_p), \quad x_p \in \mathbb{R}^{n_p}, \tag{2.5}$$

where $W_p \in \mathbb{R}^{s\times m}$ is an unknown weight matrix and $\sigma_p : \mathbb{R}^{n_p} \to \mathbb{R}^s$ is a known basis function of the form $\sigma_p(x_p)= [\sigma_{p_1}(x_p), \sigma_{p_2}(x_p), \ldots, \sigma_{p_s}(x_p)]^T$. Note for the case where the basis function $\sigma_p(x_p)$ is unknown, the parameterization in (2.5) can be relaxed [64, 65] without significantly changing the results of this paper by considering

$$\delta_p(x_p) \;=\; W_p^T \sigma_p^{nn}(V_p^T x_p) + \varepsilon_p^{nn}(x_p), \quad x_p \in \mathcal{D}_{x_p}, \tag{2.6}$$

where $W_p \in \mathbb{R}^{s\times m}$ and $V_p \in \mathbb{R}^{n_p\times s}$ are unknown weight matrices, $\sigma_p^{nn} : \mathcal{D}_{x_p} \to \mathbb{R}^s$ is a known basis composed of neural networks function approximators, $\varepsilon_p^{nn} : \mathcal{D}_{x_p} \to \mathbb{R}^m$ is an unknown residual error, and $\mathcal{D}_{x_p}$ is a compact subset of $\mathbb{R}^{n_p}$.

To address command following at the inner loop architecture, let $x_c(t) \in \mathbb{R}^{n_c}$ be the integrator state satisfying

$$\dot{x}_c(t) \;=\; E_p x_p(t) - c(t), \quad x_c(0) = x_{c_0}, \tag{2.7}$$

where $E_p \in \mathbb{R}^{n_c\times n_p}$ allows to choose a subset of $x_p(t)$ to be followed by $c(t)$. Now, (2.4) can be augmented with (2.7) as

$$\dot{x}(t) \;=\; Ax(t) + B\Lambda u(t) + BW_p^T \sigma_p(x_p(t)) + B_r c(t), \quad x(0) = x_0, \tag{2.8}$$

where

$$A \;\triangleq\; \begin{bmatrix} A_p & 0_{n_p\times n_c} \\ E_p & 0_{n_c\times n_c} \end{bmatrix} \in \mathbb{R}^{n\times n}, \tag{2.9}$$

$$B \;\triangleq\; [B_p^T, 0_{n_c\times m}^T]^T \in \mathbb{R}^{n\times m}, \tag{2.10}$$

$$B_r \;\triangleq\; [0_{n_p\times n_c}^T, -I_{n_c\times n_c}]^T \in \mathbb{R}^{n\times n_c}. \tag{2.11}$$

and $x(t) \triangleq [x_p^T(t), x_c^T(t)]^T \in \mathbb{R}^n$ is the augmented state vector, $x_0 \triangleq [x_{p_0}^T, x_{c_0}^T]^T \in \mathbb{R}^n$, and $n = n_p + n_c$. In this inner loop architecture setting, it is practically reasonable to set $Eh = [E_{\mathrm{hp}}, 0_{n_r\times n_c}]$, $E_{\mathrm{hp}} \in \mathbb{R}^{n_r\times n_p}$, in (2.3) without loss of theoretical generality since a subset of the accessible state vector is usually available and/or sensed by the human at the outer loop (but not the states of the integrator).

Finally, consider the feedback control law at the inner loop architecture given by

$$u(t) \quad = \quad u_n(t) + u_a(t), \tag{2.12}$$

where $u_n(t) \in \mathbb{R}^m$ and $u_a(t) \in \mathbb{R}^m$ are the nominal and adaptive control laws, respectively. Furthermore, let the nominal control law be

$$u_n(t) \quad = \quad -Kx(t), \tag{2.13}$$

with $K \in \mathbb{R}^{m\times n}$, such that $A_r \triangleq A - BK$ is Hurwitz. For instance, such K exists if and only if (A, B) is a controllable pair. Using (2.12) and (2.13) in (2.8) next yields

$$\dot{x}(t) \; = \; A_r x(t) + B_r c(t) + B\Lambda[u_a(t) + W^T \sigma(x(t))], \tag{2.14}$$

where $W^T \triangleq [\Lambda^{-1}W_p^T, (\Lambda^{-1} - I_{m\times m})K] \in \mathbb{R}^{(s+n)\times m}$ is an unknown aggregated weight matrix and $\sigma^T(x(t)) \triangleq [\sigma_p^T(x_p(t)), x^T(t)] \in \mathbb{R}^{s+n}$ is a known aggregated basis function. Considering (2.14), let the adaptive control law be

$$u_a(t) = -\hat{W}^T(t)\sigma(x(t)), \tag{2.15}$$

where $\hat{W}(t) \in \mathbb{R}^{(s+n)\times m}$ is the estimate of W satisfying the parameter adjustment mechanism

$$\dot{\hat{W}}(t) \quad = \quad \gamma\sigma(x(t))e^T(t)PB, \quad \hat{W}(0) = \hat{W}_0, \tag{2.16}$$

where $\gamma \in \mathbb{R}_+$ is the learning rate, and system error reads,

$$e(t) \triangleq x(t) - x_r(t), \tag{2.17}$$

with $x_r(t) \in \mathbb{R}^n$ being the reference state vector satisfying the reference system

$$\dot{x}_r(t) \quad = \quad A_r x_r(t) + B_r c(t), \quad x_r(0) = x_{r_0}, \tag{2.18}$$

and $P \in \mathbb{R}_+^{n\times n} \cap \mathbb{S}^{n\times n}$ is a solution of the Lyapunov equation

$$0 \quad = \quad A_r^T P + P A_r + R, \tag{2.19}$$

with $R \in \mathbb{R}_+^{n\times n} \cap \mathbb{S}^{n\times n}$. Since A_r is Hurwitz, it follows from [66] that there exists a unique $P \in \mathbb{R}_+^{n\times n} \cap \mathbb{S}^{n\times n}$ satisfying (2.19) for a given $R \in \mathbb{R}_+^{n\times n} \cap \mathbb{S}^{n\times n}$. Although a specific yet widely studied parameter adjustment mechanism given by (2.16) is considered, one can also consider other types of parameter adjustment mechanisms [67–80] without changing the essence of this study.

Based on the given problem formulation, the next section analyzes the stability of the coupled inner and outer loop architectures depicted in Figure 2.1 in order to establish a fundamental stability limit for guaranteeing the closed-loop system stability (when this limit is satisfied by the given human model at the outer loop and the given adaptive controller at the inner loop).

2.2 Fundamental Stability Limit

To analyze the stability of the coupled inner and outer loop architectures introduced in the previous section, the system error dynamics is derived first using (2.14), (2.15), and (2.18) as

$$\dot{e}(t) \;=\; A_r e(t) - B\Lambda \tilde{W}^T(t)\sigma(x(t)), \quad e(0) = e_0, \tag{2.20}$$

where

$$\tilde{W}(t) \triangleq \hat{W}(t) - W \in \mathbb{R}^{(s+n)\times m}, \tag{2.21}$$

is the weight error and $e_0 \triangleq x_0 - x_{r_0}$. In addition, using (2.16), the weight error dynamics is written as

$$\dot{\tilde{W}}(t) \;=\; \gamma\sigma(x(t))e^T(t)PB, \quad \tilde{W}(0) = \tilde{W}_0, \tag{2.22}$$

where $\tilde{W}_0 \triangleq \hat{W}(0) - W$. The following lemma is now immediate.

Lemma 1 *Consider the uncertain dynamical system given by (2.4) subject to (2.5), the reference model given by (2.18), and the feedback control law given by (2.12), (2.13), (2.15), and (2.16). Then, the solution* $(e(t), \tilde{W}(t))$ *is Lyapunov stable for all* $(e_0, \tilde{W}_0) \in \mathbb{R}^n \times \mathbb{R}^{(s+n)\times m}$ *and* $t \in \overline{\mathbb{R}}_+$.

Proof. To show Lyapunov stability of the solution $(e(t), \tilde{W}(t))$ given by (2.20) and (2.22) for all $(e_0, \tilde{W}_0) \in \mathbb{R}^n \times \mathbb{R}^{(s+n)\times m}$ and $t \in \overline{\mathbb{R}}_+$, consider the Lyapunov function candidate

$$\mathcal{V}(e, \tilde{W}) = e^T P e + \gamma^{-1} tr(\tilde{W}\Lambda^{\frac{1}{2}})^T(\tilde{W}\Lambda^{\frac{1}{2}}). \tag{2.23}$$

Note that $\mathcal{V}(0,0) = 0$, $\mathcal{V}(e, \tilde{W}) > 0$ for all $(e, \tilde{W}) \neq (0,0)$, and $\mathcal{V}(e, \tilde{W})$ is radially unbounded. Differentiating (2.23) along the trajectories of (2.20) and (2.22) yields

$$\dot{\mathcal{V}}(e(t), \tilde{W}(t)) = -e^T(t) R e(t) \leq 0, \tag{2.24}$$

where the result is now immediate. □

Since the solution $(e(t), \tilde{W}(t))$ is Lyapunov stable for all $(e_0, \tilde{W}_0) \in \mathbb{R}^n \times \mathbb{R}^{(s+n)\times m}$ and $t \in \overline{\mathbb{R}}_+$ from Lemma 1, this trivially implies that $e(t) \in \mathcal{L}_\infty$ and $\tilde{W}(t) \in \mathcal{L}_\infty$. At this stage of the analysis, it should be noted that one cannot use the Barbalat's lemma [81] to conclude $\lim_{t\to\infty} e(t) = 0$. To elucidate this point, one can write

$$\ddot{\mathcal{V}}(e(t), \tilde{W}(t)) = -2e^T(t) R \Big[A_r e(t) - B\Lambda\tilde{W}^T(t)\sigma(e(t) + x_r(t)) \Big], \tag{2.25}$$

where since $x_r(t)$ can be unbounded due to the coupling between the inner and outer loop architectures, one cannot conclude the boundedness of (2.25), which is necessary for utilizing the Barbalat's lemma in (2.24). Motivated from this standpoint, the conditions to ensure the boundedness of the reference model states $x_r(t)$ are provided, which also reveal the fundamental stability limit (FSL) for guaranteeing the closed-loop system stability. Using (2.2) in (2.18), it can be written that

$$\begin{aligned} \dot{x}_r(t) &= A_r x_r(t) + B_r(C_h\xi(t) + D_h\theta(t-\tau)), \\ &= A_r x_r(t) - B_r D_h E_h x_r(t-\tau) + B_r C_h \xi(t) - B_r D_h E_h e(t-\tau) \\ &\qquad + B_r D_h r(t-\tau). \end{aligned} \tag{2.26}$$

Next, it follows from (2.1) that

$$\dot{\xi}(t) = Ah\xi(t) - B_h E_h x_r(t-\tau) - B_h E_h e(t-\tau) + B_h r(t-\tau). \tag{2.27}$$

Finally, by letting $\phi(t) \triangleq [x_r^T(t), \xi^T(t)]^T$, and using (2.26) and (2.27), one can write

$$\dot{\phi}(t) \;=\; \mathcal{A}_0\phi(t) + \mathcal{A}_\tau\phi(t-\tau) + \varphi(\cdot), \quad \phi(0) = \phi_0, \tag{2.28}$$

where

$$\mathcal{A}_0 \triangleq \begin{bmatrix} A_r & B_rC_h \\ 0_{n_\xi\times n} & A_h \end{bmatrix} \in \mathbb{R}^{(n+n_\xi)\times(n+n_\xi)}, \tag{2.29}$$

$$\mathcal{A}_\tau \triangleq \begin{bmatrix} -B_rD_hE_h & 0_{n\times n_\xi} \\ -B_hE_h & 0_{n_\xi\times n_\xi} \end{bmatrix} \in \mathbb{R}^{(n+n_\xi)\times(n+n_\xi)}, \tag{2.30}$$

$$\varphi(\cdot) \triangleq \begin{bmatrix} -B_rD_hE_he(t-\tau) + B_rD_hr(t-\tau) \\ -B_hE_he(t-\tau) + B_hr(t-\tau) \end{bmatrix} \in \mathbb{R}^{n+n_\xi}. \tag{2.31}$$

As a consequence of Lemma 1 and the boundedness of the reference $r(t)$, one can conclude that $\varphi(\cdot) \in \mathcal{L}_\infty$. Next, the following lemma is provided:

Lemma 2 *Consider the following system dynamics given by*

$$\dot{z}(t) = Fz(t) + Gz(t-\tau) + h(t, z(t)), \quad z(0) = z_0, \tag{2.32}$$

where $z(t) \in \mathbb{R}^n$ is the state vector, $F \in \mathbb{R}^{nxn}$ and $G \in \mathbb{R}^{nxn}$ are constant matrices, τ is the time delay and $h(t, z(t))$ is piecewise constant and bounded nonlinear forcing term, which is in general a function of state z. If the homogeneous dynamical system given by

$$\dot{z}(t) = Fz(t) + Gz(t-\tau) \tag{2.33}$$

is asymptotically stable, then the states of the original inhomogeneous dynamical system given by (2.32) *remains bounded for all times.*

Proof. Since $h(t, z(t))$ is piecewise continuous and bounded, this signal can be considered as an exogenous input to the system with the transfer function

$$G(s) = \Big(sI - (F + Ge^{-\tau s})\Big)^{-1}. \tag{2.34}$$

Under the assumption that the homogeneous system (2.33) is asymptotically stable, then all of the infinitely many roots of the characteristic equation are known

$$\det\Big(sI - (F + Ge^{-\tau s})\Big) = 0, \tag{2.35}$$

of the system (2.34), have strictly negative real parts. Therefore, the output $z(t)$ of the dynamical system remains bounded. □

Theorem 1 *Consider the uncertain dynamical system given by (2.4) subject to (2.5), the reference model given by (2.18), the feedback control law given by (2.12), (2.13), (2.15), and (2.16), and the human dynamics given by (2.1), (2.2), and (2.3). Then,* $e(t) \in \mathcal{L}_\infty$ *and* $\tilde{W}(t) \in \mathcal{L}_\infty$*. If, in addition, the real parts of all the infinitely many roots of the following characteristic equation*

$$det\Big(sI - (\mathcal{A}_0 + \mathcal{A}_\tau e^{-\tau s})\Big) = 0, \tag{2.36}$$

have strictly negative real parts, then $x_r(t) \in \mathcal{L}_\infty$, $\xi(t) \in \mathcal{L}_\infty$, *and* $\lim_{t\to\infty} e(t) = 0$.

Proof. As a consequence of Lemma 1, recall that $e(t) \in \mathcal{L}_\infty$ and $\tilde{W}(t) \in \mathcal{L}_\infty$. In addition, note that $\varphi(\cdot) \in \mathcal{L}_\infty$ in (2.28). Therefore, if all of the roots of the characteristic equation given by (2.36) have strictly negative real parts, making the homogeneous equation

$$\dot{\phi}(t) = \mathcal{A}_0\phi(t) + \mathcal{A}_\tau\phi(t-\tau) \tag{2.37}$$

asymptotically stable, then, per Lemma 2, $\phi(t) \triangleq [x_r^T(t), \xi^T(t)]^T \in \mathcal{L}_\infty$. Finally, since $e(t) \in \mathcal{L}_\infty$, $x_r(t) \in \mathcal{L}_\infty$, and $\tilde{W}(t) \in \mathcal{L}_\infty$ ensure the boundedness of (2.25), it now follows from the Barbalat's lemma that $\lim_{t\to\infty} e(t) = 0$. □

Note that there are several methods in the literature for the analysis of the root locations of (2.36). The four most-used methods are TRACE-DDE [82], DDE-BIFTOOL [83], QPMR [84], and Lambert-W function [85]. In essence, one provides the matrices $\mathcal{A}_0$ and $\mathcal{A}_\tau$ as well as the delay τ to these methods, which then return the numerical values of the rightmost root locations of (2.36). In some sense, these methods perform a nontrivial approximation with which they are able to identify the most relevant roots — the rightmost roots. In the illustrative numerical example provided below, TRACE-DDE is employed, readily available for download at `https://users.dimi.uniud.it/~dimitri.breda/research/software/`.

Lemma 3 *Consider the control error $e(t)$ in Eqn. (2.17) with Laplace transform $\mathcal{E}(s)$ and $r(t)$ with Laplace transform $R(s)$ as the reference input. Then, the human error $\theta(t)$ in Eqn. (2.3) is determined in Laplace domain by*

$$\Theta(s) = (I + E_h G_1)^{-1} R(s) - (I + E_h G_1)^{-1} E_h \mathcal{E}(s), \tag{2.38}$$

where

$$G_1 \triangleq (sI - A_r)^{-1}(B_r C_h (sI - A_h)^{-1} B_h + B_r D_h) e^{-\tau s}. \tag{2.39}$$

Proof. Considering the human dynamics given by Eqn. (2.1) and Eqn. (2.2), and reference model dynamics given by Eqn. (2.18), one can write

$$X_r(s) = (sI - A_r)^{-1} B_r (C_h \xi(s) + D_h e^{-\tau s} \Theta(s)). \tag{2.40}$$

Moreover, notice that, using Eqn. (2.1), it can be written that

$$\xi(s) = (sI - A_h)^{-1} B_h e^{-\tau s} \Theta(s). \tag{2.41}$$

Hence, combining Eqn. (2.40) and Eqn. (2.41), transfer function G_1 in Eqn. (2.39) follows. Next, with human error defined as

$$\theta(t) = r(t) - E_h x(t), \tag{2.42}$$

and, considering the error equation given by (2.17),

$$\theta(t) = r(t) - E_h x_r(t) - E_h e(t). \tag{2.43}$$

By simple manipulations, Eqn. (2.38) follows. $\square$

Table 2.1: Numerical data used in illustrative numerical example

T_z	1
T_p	5
k_p	5
τ	0.5
A_p	$\begin{bmatrix} -0.0030 & 0.0390 & 0 & -0.3220 \\ -0.0650 & -0.3190 & 7.7400 & 0 \\ 0.0201 & -0.1010 & -0.4290 & 0 \\ 0 & 0 & 1 & 0 \end{bmatrix}$
B_p	$[0.0100 \quad -0.1800 \quad -1.1600 \quad 0]^T$
E_p	$[0 \quad 0 \quad 0 \quad 1]$
E_h	$[0 \quad 0 \quad 0 \quad 1 \quad 0]$
B_r	$[0 \quad 0 \quad 0 \quad 0 \quad 1]^T$
Q	$\mathrm{diag}([0 \quad 0 \quad 0 \quad 1 \quad 2.5])$

Notice that the relationship between $\theta(t)$, $r(t)$, and $e(t)$ is important for two reasons. Firstly, it allows to estimate the steady state error in $\theta(t)$ given $r(t)$ since $\lim_{t\to\infty} e(t) \to 0$, when the system is stable. Secondly, even if MRAC is properly designed, and its error dynamics $e(t)$ goes to zero in steady state, this dynamics can influence the human error dynamics $\theta(t)$ in an undesirable way. Specifically, certain frequency content in $e(t)$ may excite $\theta(t)$ causing poor performance at the human end.

Based on the given problem formulation, the next section analyzes the stability of the closed-loop system depicted in Fig. 2.1 for various filter parameters to study the performance of MRAC-human and MRAC-human-filter dynamics as well as to better understand the error dynamics $\Theta(s)$ in (2.38).

2.3 Illustrative Numerical Example

Consider the longitudinal motion of a Boeing 747 airplane linearized at an altitude of 40 kft and a velocity of 774 ft/sec with the dynamics given by [86]

$$\dot{x}(t) = A_p x(t) + B_p(u(t) + W^T \sigma(x(t))), \quad x(0) = x_0, \tag{2.44}$$

where $x(t) = [x_1(t),\ x_2(t),\ x_3(t),\ x_4(t)]^T$ is the state vector. Note that (2.44) can be equivalently written as (2.4) with $\Lambda = I$. Here, $x_1(t)$, $x_2(t)$, and $x_3(t)$ respectively represent the components of the velocity along the x, z and y axes of the aircraft with respect to the reference axes (in crad/sec), and $x_4(t)$ represents the pitch Euler angle of the aircraft body axis with respect to the reference axes (in crad). Recall that 0.01 radian = 1 crad (centriradian). In addition, $u(t) \in \mathbb{R}$ represents the elevator control input (in crad). Finally, $W \in \mathbb{R}^3$ is an unknown weighting matrix and $\sigma(x(t)) = [1,\ x_1(t),\ x_2(t)]^T$ is a known basis function. In the following simulations, $W = [0.1 \quad 0.3 \quad -0.3]^T$. The dynamical system given in (2.44) is assumed to be controlled using a model reference adaptive controller, the details of which are explained in Section 2.1. In addition, the aircraft is assumed to be operated by a pilot whose Neal-Schmidt Model [4] is given by

$$G_h = k_p \frac{T_p s + 1}{T_z s + 1} e^{-\tau s}, \tag{2.45}$$

where k_p is the positive scalar pilot gain, T_p and T_z are positive scalar time constants, and τ is the pilot reaction time delay. The values of the parameters used in the simulations are provided in Table 2.1. Consider next a linear filter of the form

$$G_f = \frac{F_1 s + 1}{F_2 s + 1}, \tag{2.46}$$

attached in series to the human model, when necessary, as shown in Fig. 2.1, where scalars F_1 and F_2 are filter time constants. In this case, human-filter transfer function becomes

$$G_{h,f} = k_p e^{-\tau s} \frac{T_z s + 1}{T_p s + 1} \frac{F_1 s + 1}{F_2 s + 1}, \tag{2.47}$$

which is equivalent to the human-filter state space in Eqn. (2.1) and Eqn. (2.2).

To obtain the nominal controller K, a linear quadratic regulator (LQR) approach is utilized with the following objective function to be minimized

$$J(\cdot) = \int_0^\infty (x^T(t) Q x(t) + \mu u^2(t)) dt, \tag{2.48}$$

where Q is a positive-definite weighting matrix of appropriate dimension and μ is a positive weighting scalar. Notice that the framework developed in Section 2.1

is not limited to a particular design method for the nominal controller. To this end, this task can be handled by a number of different ways. Here LQR is utilized for convenience reasons. In this setting, the selection of the weighing matrices, as expected, will affect the resulting nominal controller gain K in (2.13), which in turn will determine the reference model dynamics (2.18). In the following simulation studies, the effect of the weighting matrices, and thus the effects of reference model parameters on system stability are investigated for various values of pilot model parameters. To facilitate the analysis, reference model parameter variations is achieved mainly by manipulating the control penalty variable μ.

Note that the purpose of the numerical examples provided in this section is to verify the theoretical stability predictions of the proposed framework. Therefore, the simulation results are created to present the stability/instability of the closed loop system without paying attention to enhanced transient response characteristics.

2.3.1 Effect of Control Penalty on System Stability for Different Pilot Reaction Time Delays

To investigate the effects of the reference model parameter variations on the stability of the closed loop system, the control weight μ is manipulated by assigning values in the range [0, 50]. Then, the rightmost pole (RMP) of the system, whose characteristic equation is given by (2.36), is plotted against these μ values. This procedure is repeated for various pilot reaction time delays and the results are presented in Figure 2.2.

Figure 2.2 reveals several interesting results. First, it is shown that if the reference model dynamics is not chosen carefully with an appropriate μ value, then the human-in-the-loop adaptive control system can be indeed unstable. Second, it is seen that the closed loop system can be stable for small and large values of the parameter μ and be unstable in between. Third, it is observed that as the pilot reaction time delay increases, the unstable region of μ gets larger as

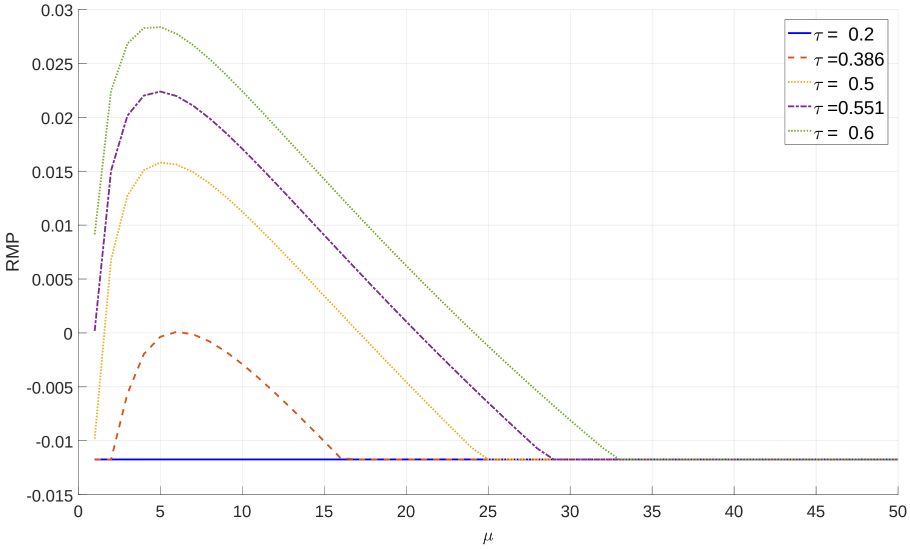

Figure 2.2: The location of the right most pole of (2.37) with respect to the control penalty variable μ, for different pilot reaction time delays.

indicated by $RMP > 0$.

It is predicted in Figure 2.2 that for $\mu = 10$, pilot reaction time delays $\tau = 0.2$ and $\tau = 0.5$ results in a stable and unstable system, respectively. Time domain tracking and control signal plots presented in Figure 2.3 confirm this prediction. As noted earlier, the simulation results are employed to verify the theoretical stability predictions of the proposed method and therefore controllers are not tuned to obtain the best transient response. The investigation of the effect of the human-controller interactions on the transient response will be addressed in future research.

2.3.2 Effect of Control Penalty on System Stability for Different Values of Pilot Model Poles

The poles of the pilot model (2.45) represent how fast the pilot responds to changes in the aircraft pitch angle, which can also be interpreted as pilot aggressiveness. In this section, the effect of pilot aggressiveness on system stability is

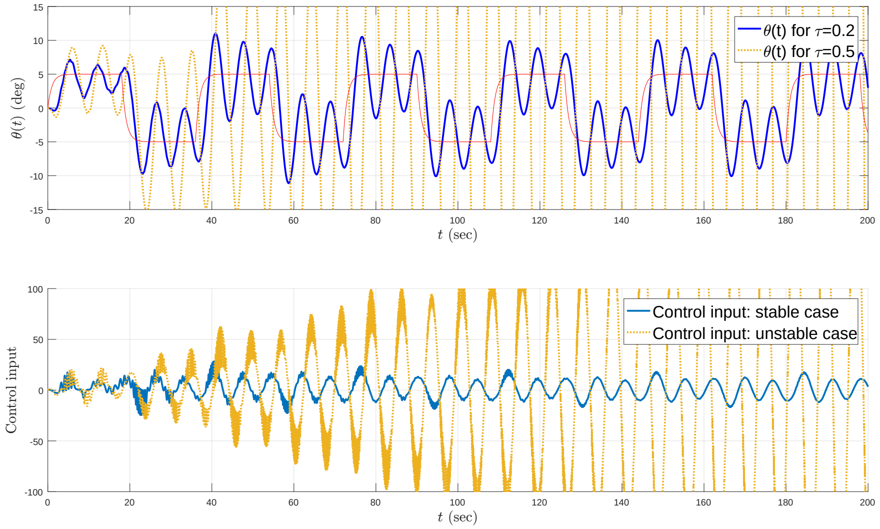

Figure 2.3: Tracking and control signal curves for two different values of the pilot reaction time delays, $\tau = 0.2$ and $\tau = 0.5$, when $\mu = 10$.

investigated while assigning values to the control penalty μ from 0 to 50.

Figure 2.4 depicts the effect of the pilot pole locations on the RMP. The zero location and the time-delay of the pilot model, are kept at their nominal values of -1 and 0.5, respectively. It is seen from the figure that, in general, unstable-stable-unstable transition is observed for increasing values of μ and, as expected, higher values of poles, corresponding to faster pilot response, decrease the μ region of stability. Figure 2.5 depicts the tracking and control signal curves for two pilot model pole locations; that is, -0.175 and -0.2, when $\mu = 10$. As predicted in Figure 2.4, the closed loop system remains stable when the pole is located at -0.175 and becomes unstable when the pole is at -0.2.

2.3.2.1 Effect of Control Penalty on System Stability for Different Values of Pilot Model Zeros

In this section, the effect of zeros of the pilot transfer function (2.45) on system stability is investigated when control penalty μ takes values in the range [0,50].

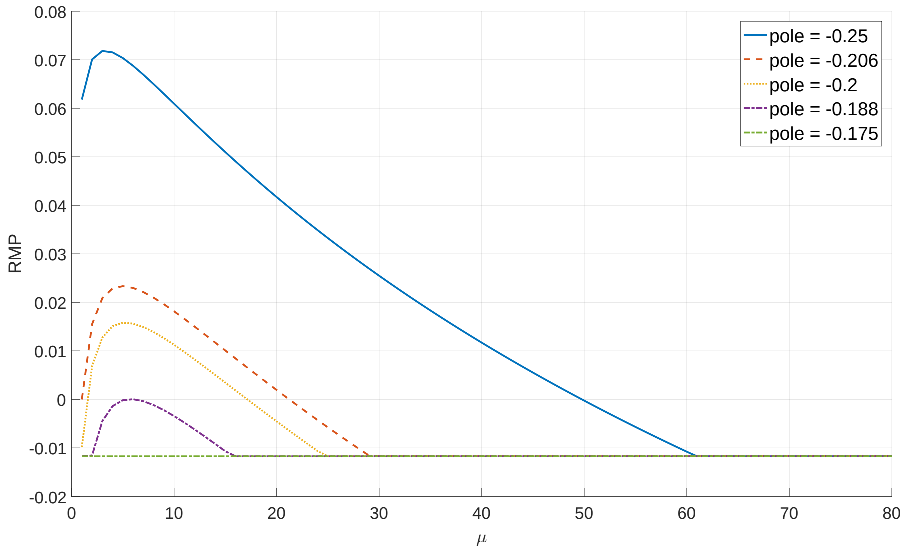

Figure 2.4: The location of the right most pole of (2.37) with respect to the control penalty variable μ, for different pilot transfer function pole locations.

The pole location and the time delay of the pilot transfer function are kept at their nominal values of -0.2 and 0.5, respectively. Changes in the zero location of the model can be interpreted as an adjustment to the "lead" nature of the pilot, which is related to pilot's anticipation capabilities.

As seen in Figure 2.6, stable-unstable-stable transition structure still exists, in general, for increasing μ values. Furthermore, it is seen that when the pilot transfer function does not have a zero, a large μ region of instability arises.

It is noted that for the given nominal values of the system parameters, no value of zero can make the system always stable, regardless of the μ value, since delay-independence is determined only by the pilot's gain k_p.

Figure 2.7 presents tracking and control signal curves for pilot model zero locations -0.2 and -0.909, for the case when $\mu = 1$. As predicted in Figure 2.6, the closed loop system becomes stable for the former and unstable for latter zero value.

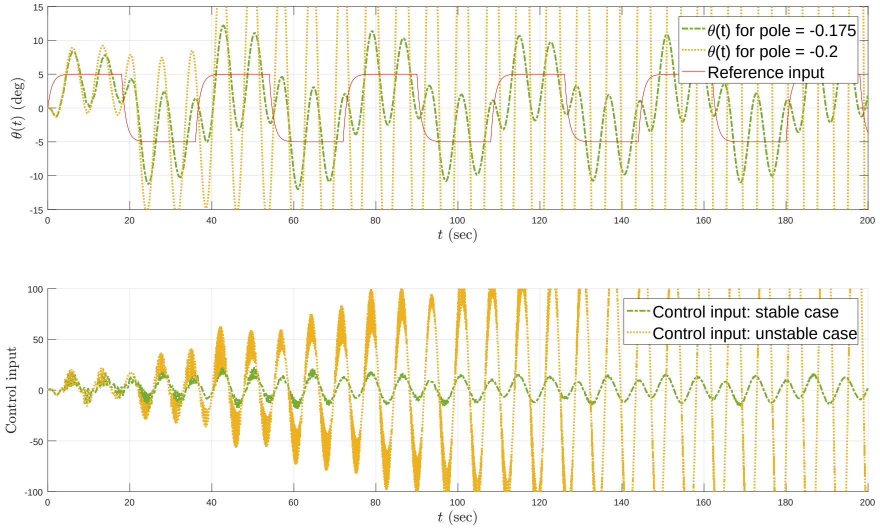

Figure 2.5: Tracking and control signal curves for two different values of the pilot transfer function pole locations, $p = -0.175$ and $p = -0.2$, when $\mu = 10$.

2.3.3 Effect of Control Penalty on System Stability for Different Values of Pilot Model Gains

The pilot gain in k_p in (2.45) determines the intensity of the response that the pilot gives to the pitch angle deviations in the aircraft. In some sense, this gain also represents the aggressiveness of the pilot.

Stability properties of the pilot-in-the-loop system depending on the nominal control penalty μ and the pilot gain k_p is presented in Figure 2.8, where the RMP vs μ is plotted for certain values of k_p. In these analyses, the pole and zero locations and time-delay of the pilot transfer function are kept at their nominal values of -0.2, -1, and 0.5, respectively. From the figure, stable-unstable-stable stability transition is once again observed for increasing values of μ. On the other hand, it is seen that, similar to the trend for the pilot pole location, as the pilot gain increases, the μ stability region shrinks. These results confirm the well-known adverse effects of high gain of pilots on system stability, such as pilot-induced oscillations [25, 45, 87].

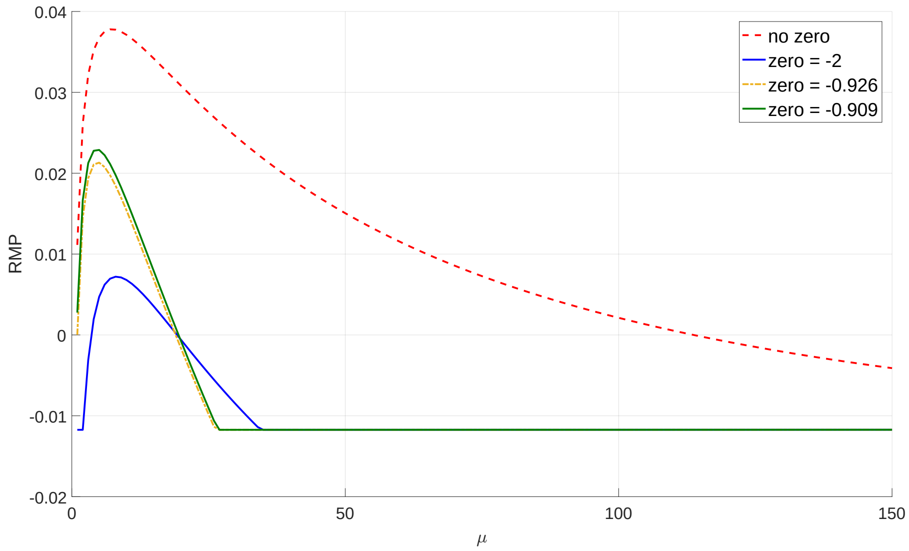

Figure 2.6: The location of the right most pole of (2.37) with respect to the control penalty variable μ, for different pilot transfer function zero locations.

It is predicted in Figure 2.8 that the closed loop system will be stable for $k_p = 4$ and unstable for $k_p = 5$, when $\mu = 10$. This is confirmed by the results presented in Figure 2.9, where time domain tracking and control signal curves are plotted for these gain values.

2.3.4 Human-Pilot Dynamics with a Linear Filter

To study the effects of the filter on the stability of the nominal linear closed-loop system Eqn. (2.28) with $\varphi(\cdot) = 0$, the real part of the rightmost pole (RMP) of this system is first computed using TRACE-DDE on the plane of the filter parameters F_1 and F_2. Fig. 2.10 depicts the effect of F_1 and F_2 on the location of RMP, where only blue areas indicate stability with negative real part of the rightmost pole, RMP< 0. In this figure, it can be seen that to avoid the boundary of instability when RMP $= 0$, the condition of $F_2 > F_1$ needs to be satisfied; therefore, lag compensator, which is essentially a low-pass filter is needed (see, for example, [88]).

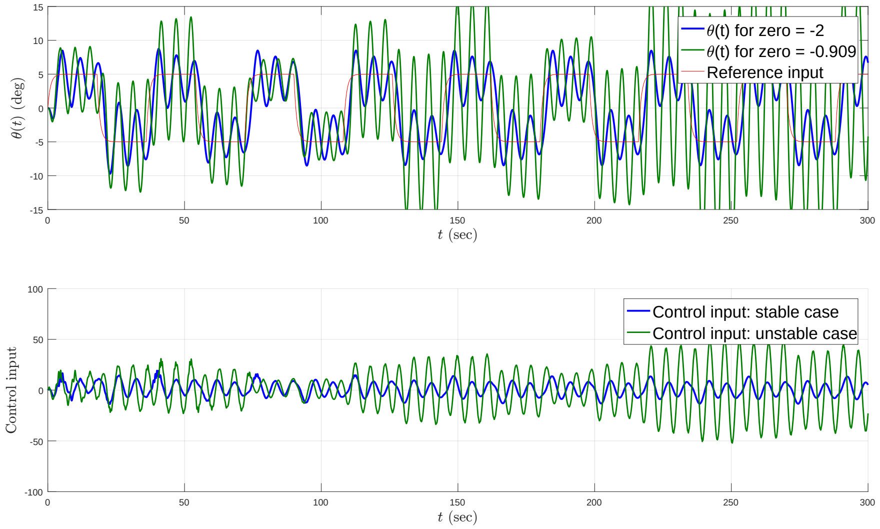

Figure 2.7: Tracking and control signal curves for two different values of the pilot transfer function zero locations, $z = -2$ and $z = -0.909$, when $\mu = 10$.

To decide on the optimal F_1 and F_2 values, and explore them in a larger range, Simulated Annealing (SA) method is incorporated next (see, for example, [89–91]). The optimization or energy function for this case is considered to be

$$J_{SA} = RMP, \tag{2.49}$$

as this study concerns the stability of the system. The method is initialized from an unstable point with $F_1 = F_2 = 1$, which corresponds to no-filter case. Fig. 2.11 depicts how Simulated Annealing finds the optimal filter parameters, which are $F_1 = 71.448$ and $F_2 = 152.051$. As the iterations progress, it is observed that in most of the steps, $F_2 > F_1$, indicating consistency with the initial findings in Fig. 2.10. For this filter parameters, RMP is computed to be $= -0.012$. One point to note is that in designing the filter parameters using simulated annealing, one has to be careful that A_r of the reference model remains Hurwitz, otherwise it will violate the conditions of Theorem 1 and will result in instability of inner loop, and therefore instability the overall close-loop system. This is the reason why the filter cannot optimize the the energy function (2.49) further especially for higher values of μ (see Fig. 2.12).

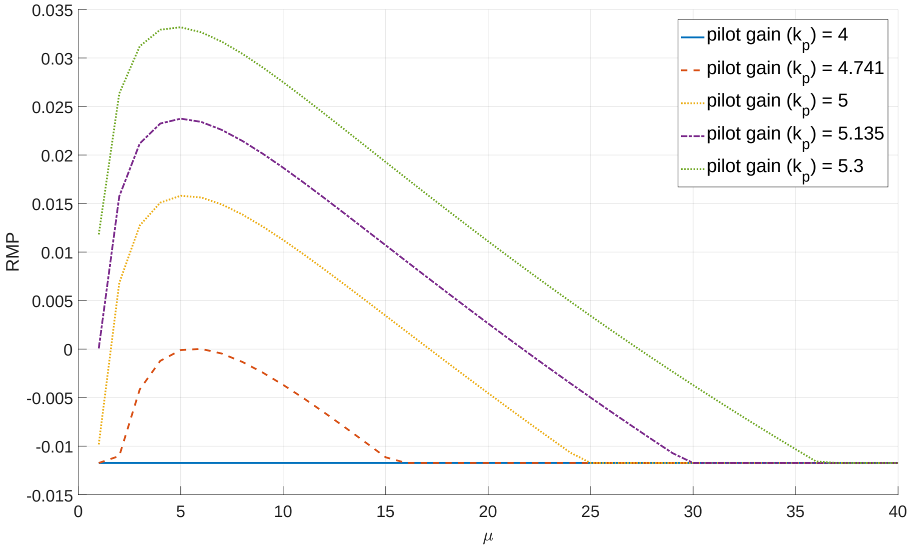

Figure 2.8: The location of the right most pole of (2.37) with respect to the control penalty variable μ, for different pilot transfer function gain values.

One key utility of the designed filter is that it is possible to stabilize an unstable MRAC-human closed-loop system. Specifically, considering Fig. 2.12, one can see that with the value of $\mu = 15$ and pilot model settings as in Table 2.1, the nonlinear closed-loop system is unstable; and, when the linear filter with the parameters obtained by simulated annealing method is inserted in the closed-loop system, stability can be recovered. Fig. 2.13 and its zoom-in version in Fig. 2.14 depict the time domain response of the system, for both unstable and stabilized systems[1]. Note that the filter is ineffective on the stability of the closed-loop system for $\mu > 22$, although it improves the transience, see Fig. 2.15.

Moreover, as previously mentioned, LQR method is used to design the nominal controller K in (2.13). Since $A_r = A - BK$, the designed K will determine the reference model dynamics. As shown in Fig. 2.12, for the values of $\mu < 20$, prescribed performance for a given A_r matrix is not attainable, since the overall system becomes unstable; for example, as Figure 2.16 depicts, attaining faster reference system, i.e. rise of the reference system $t_r < 3.423$ seconds, is not

---

[1] It is worth noting that for the sake of consistency, an unstable case is selected for the without-filter plots, that was stabilized using linear filter.

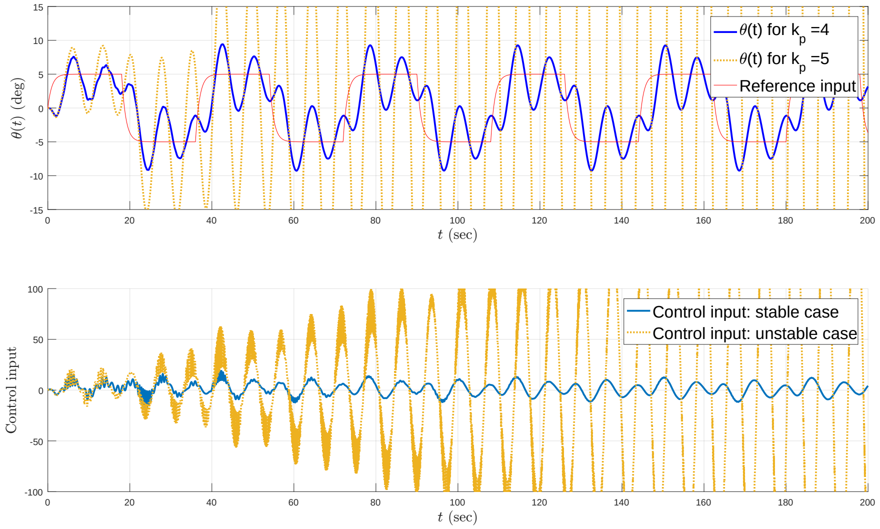

Figure 2.9: Tracking and control signal curves for two different values of the pilot transfer function gain values, $k_p = 4$ and $k_p = 5$, when $\mu = 10$.

feasible with the current structure; but, by simply inserting a linear filter, faster reference system performance becomes attainable.

2.3.5 Human error vs. MRAC error

As discussed in the stability analysis, it is critical to study how human error $\Theta(s)$ is related to the control error signal $\mathcal{E}(s)$. Therefore, the effect of the presence of a linear filter on this relationship is next studied. Fig. 2.17 depicts the Bode plots of the transfer function derived in (2.38), assuming $R(s) = 0$, for the same pilot model settings as in Table 2.1. Here, it is observed that the filter suppresses undesired peak of 35.854 dB at $\omega = 0.800$ rad/sec down to 6.191 dB at $\omega = 0.71$ rad/sec, achieving a 26.663 dB reduction. This indicates that any excitation from MRAC error dynamics $e(t)$ on $\theta(t)$ error of the human at $\omega = 0.8$ rad/sec can be reduced more than an order of magnitude, thereby causing much less detrimental effects on the human error dynamics when a lag filter is utilized within the MRAC scheme.

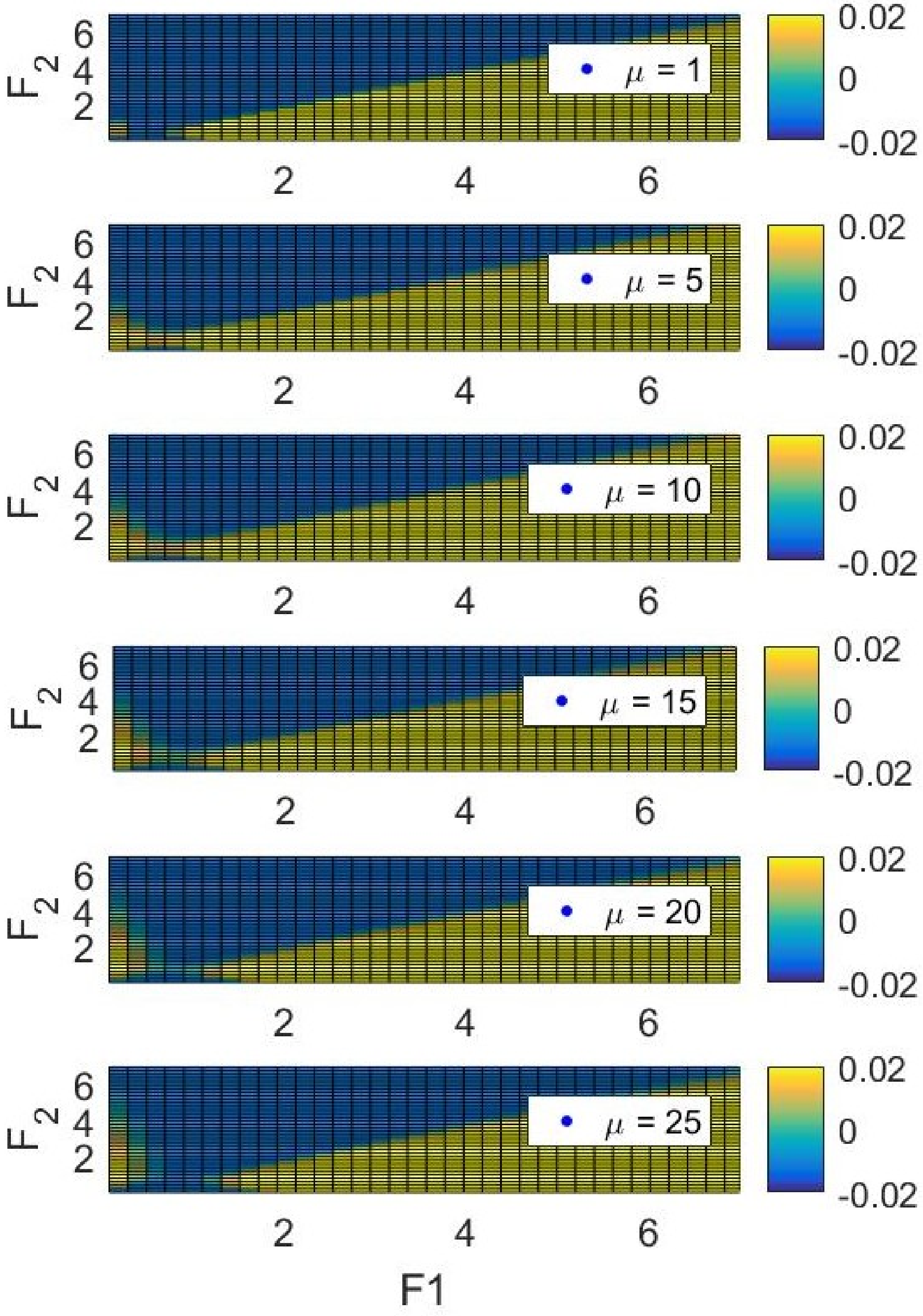

Figure 2.10: Comparison of the effect of F_1 and F_2 on the color-coded real part of the rightmost pole (RMP) of the nominal linear system for different penalty gains μ of LQR. the system is stable for RMP < 0, otherwise unstable.

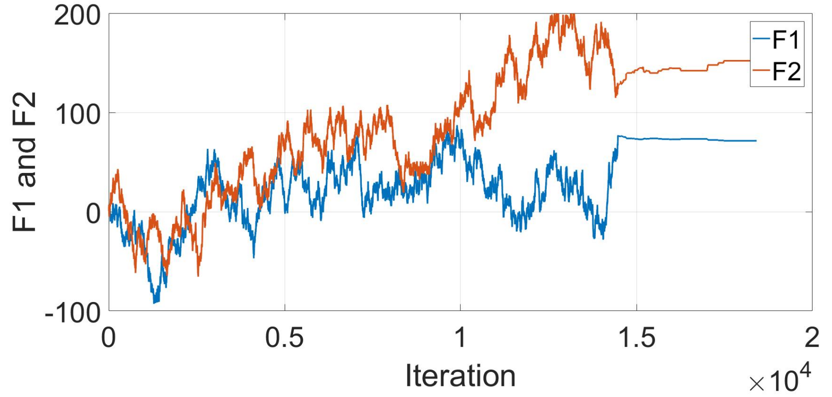

Figure 2.11: F_1 and F_2 Vs. iterations of the simulated annealing method.

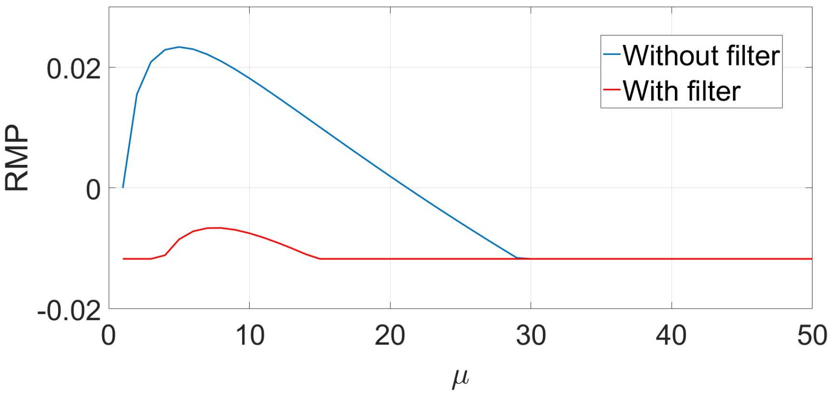

Figure 2.12: The effect of designed linear filter on stability of the linear nominal system with respect to penalty gain μ of LQR.

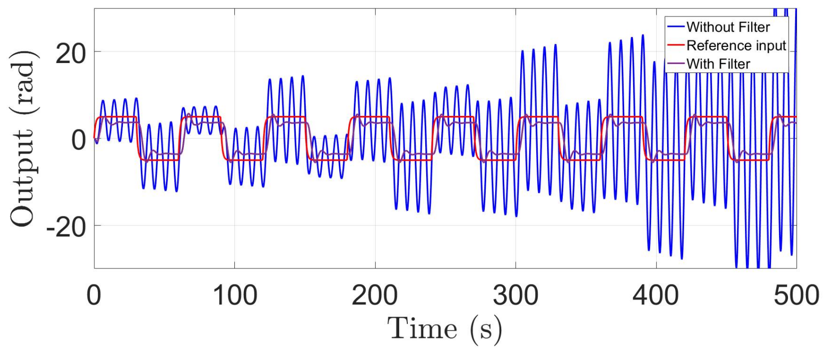

Figure 2.13: Response of the closed-loop nonlinear system with and without using the designed linear filter for $\mu = 15$.

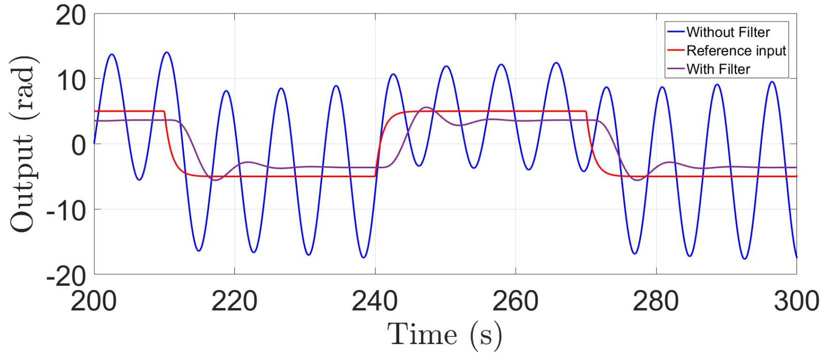

Figure 2.14: Close-up response of the closed-loop nonlinear system obtained in Fig. 2.13.

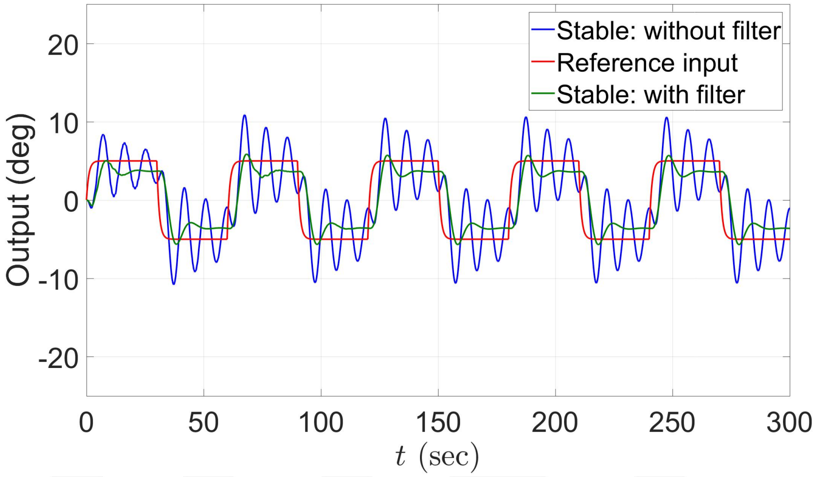

Figure 2.15: Response of the closed-loop nonlinear system with and without using the designed linear filter for $\mu = 40$.

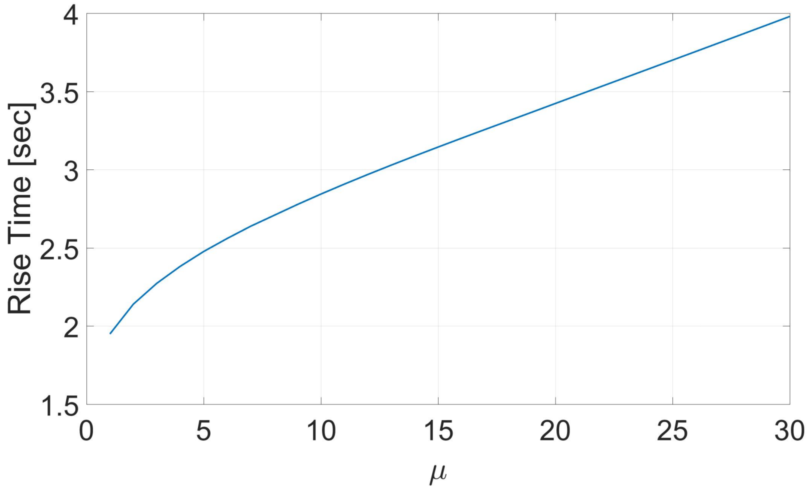

Figure 2.16: Change of the rise time (t_r) of the reference system with respect to the penalty gain μ.

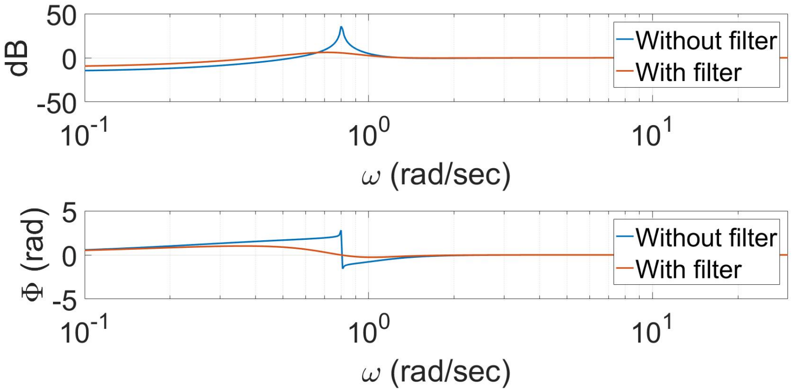

Figure 2.17: Bode plots of the transfer function between the input $\mathcal{E}(s)$ and output $\Theta(s)$ derived in (2.38) for the case with and without the designed linear filter. Here reference input $R(s)$ is assumed to be zero.

Chapter 3

Stability of Human-in-the-Loop Telerobotics in the Presence of Time-Delays

In this chapter, stability of various architectures of human-in-the-loop telerobotic system with force feedback and communication delays is investigated. A general linear time-invariant time-delayed mathematical model of the human operator is incorporated into the system dynamics based on the interaction of the human operator with the rest of the telerobotic system. The resulting closed loop dynamics contains two independent time-delays mainly due to back and forth communication delay and human reaction time delay. Stability of this dynamics is characterized next on the plane of the two delays by rigorous mathematical investigation using Cluster Treatment of Characteristic Roots (CTCR). An illustrative numerical example is further provided in the results section along with interpretations.

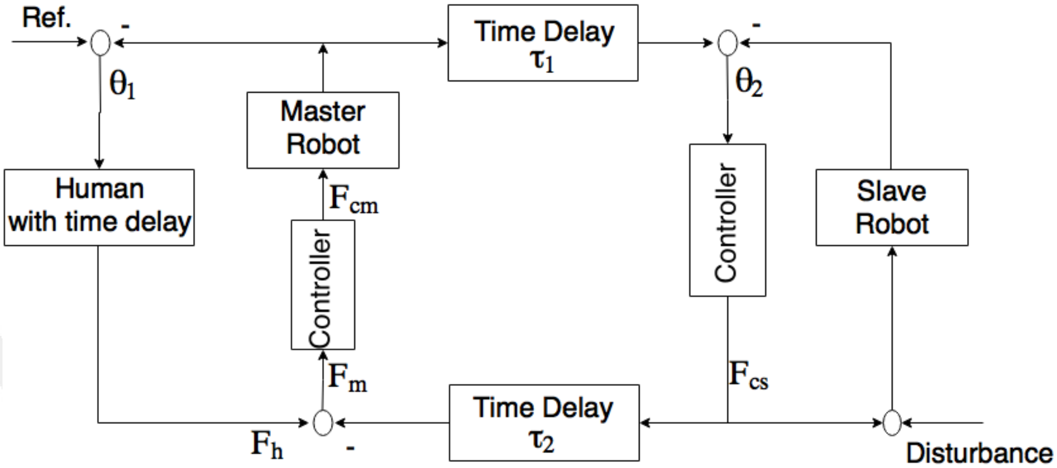

Figure 3.1: Block Diagram of the overall human-in-the-loop telerobotic: *baseline* when the controller = 1; otherwise: *configuration 1*.

3.1 Problem Formulation

3.1.1 Baseline

3.1.1.1 Baseline System Analysis

The human-in-the-loop telerobotic system shown in Figure 3.1 depicts the baseline architecture when the controller = 1 in the frequency domain. This architecture is assumed to be in free motion state (disturbance = 0) Specifically, a human operator with the following linear time-invariant model is considered in the closed-loop analysis,

$$\dot{x}_h(t) = A_h x_h(t) + B_h \theta_1(t - \tau_h), \quad x_h(0) = 0 \tag{3.1}$$

$$F_h(t) = C_h x_h(t) + D_h \theta_1(t - \tau_h), \tag{3.2}$$

where $x_h(t) \in \mathbb{R}^{n_h}$ is the human state vector, $\tau_h \in \mathbb{R}^+$ is the human reaction time-delay, $A_h \in \mathbb{R}^{n_h \times n_h}$, $B_h \in \mathbb{R}^{n_h \times n_{\theta_1}}$, $C_h \in \mathbb{R}^{n_{F_h} \times n_h}$, and $D_h \in \mathbb{R}^{n_{F_h} \times n_{\theta_1}}$ are "human operator system" matrices, and $F_h(t) \in \mathbb{R}^{n_{F_h}}$ is the human operator's force command. The input to the human dynamics is given by

$$\theta_1 \triangleq r(t) - y_m(t), \tag{3.3}$$

where $\theta_1(t) \in \mathbb{R}^{n_r}$ is the error vector with $r(t) \in \mathbb{R}^{n_r}$ defined as the reference input, and $y_m(t)$ as the output of the master robot.

Master robot is considered to be a system with the following dynamics

$$\begin{align}\dot{x}_m(t) &= A_m x_m(t) + B_m F_m(t), \quad x_m(0) = 0 \tag{3.4}\\ y_m(t) &= C_m x_m(t) + D_m F_m(t), \tag{3.5}\end{align}$$

where $x_m(t) \in \mathbb{R}^{n_m}$ is the master robot state vector, $y_m(t) \in \mathbb{R}^{n_{ym}}$ is the output of the master robot, and $A_m \in \mathbb{R}^{n_m \times n_m}$, $B_m \in \mathbb{R}^{n_m \times n_{F_m}}$, $C_m \in \mathbb{R}^{n_{ym} \times n_m}$, and $D_m \in \mathbb{R}^{n_{ym} \times n_{F_m}}$ are the master robot system matrices. $F_m(t) \in \mathbb{R}^{n_{F_h}}$ is the force input applied to the master robot, given by

$$F_m(t) = F_h(t) - F_c(t - \tau_2), \tag{3.6}$$

where $F_c(t)$ is the output of the slave-side controller, and $\tau_2 \in \mathbb{R}^+$ is the feedback communication time-delay.

The slave robot dynamics is governed by

$$\begin{align}\dot{x}_s(t) &= A_s x_s(t) + B_s F_c(t), \quad x_s(0) = 0 \tag{3.7}\\ y_s(t) &= C_s x_s(t) + D_s F_c(t), \tag{3.8}\end{align}$$

where $x_s(t) \in \mathbb{R}^{n_s}$ is the slave robot state vector, $y_s(t) \in \mathbb{R}^{n_{ys}}$ is the output of the slave robot, and $A_s \in \mathbb{R}^{n_s \times n_s}$, $B_s \in \mathbb{R}^{n_s \times n_{F_c}}$, $C_s \in \mathbb{R}^{n_{ys} \times n_s}$, and $D_s \in \mathbb{R}^{n_{ys} \times n_{F_c}}$ are the slave robot system matrices.

The slave-side controller dynamics is in the following general form

$$\begin{align}\dot{x}_c(t) &= A_c x_c(t) + B_c \theta_2(t), \quad x_c(0) = 0 \tag{3.9}\\ F_c(t) &= C_c x_h(t) + D_c \theta_2(t), \tag{3.10}\end{align}$$

where $x_c(t) \in \mathbb{R}^{n_c}$ is the controller state vector, and $A_c \in \mathbb{R}^{n_c \times n_c}$, $B_c \in \mathbb{R}^{n_c \times n_{\theta_2}}$, $C_c \in \mathbb{R}^{n_{F_c} \times n_c}$, and $D_s \in \mathbb{R}^{n_{F_c} \times n_{\theta_2}}$ are the controller system matrices. The tracking error on the slave side is given as

$$\theta_2(t) \triangleq y_m(t - \tau_1) - y_s(t), \tag{3.11}$$

where $\theta_2(t) \in \mathbb{R}^{n_{ym}}$, and $\tau_1 \in \mathbb{R}^+$ is the feedforward communication time-delay.

3.1.1.2 Baseline Stability Analysis

Using (3.3) and (3.5), one obtains

$$\theta_1(t) \triangleq r(t) - C_m x_m(t), \tag{3.12}$$

and using (3.5), (3.8), and (3.11), the slave side tracking error is expressed as

$$\theta_2(t) = G_0 C_m x_m(t-\tau_1) - G_0 C_s x_s - G_0 D_s C_c x_c, \tag{3.13}$$

where the existence of $G_0 = (I + D_s D_c)^{-1}$ is assumed implicitly. Considering (3.2), (3.6), and (3.9), it can be written that

$$F_m(t) = C_h x_h(t) + D_h \theta_1(t-\tau_h) - C_c x_c(t-\tau_2) - D_c \theta_2(t-\tau_2). \tag{3.14}$$

By letting $\phi(t) \triangleq [x_h^T(t), x_m^T(t), x_c^T(t), x_s^T(t)] \in \mathbb{R}^n$, and using (3.4), (3.7), (3.9), (3.12), (3.13) and (3.14), the augmented state space representation of the dynamics in Figure 3.1 is obtained as

$$\dot{\phi}(t) = \mathcal{A}_0 \phi(t) + \mathcal{A}_{\tau_h} \phi(t-\tau_h) + \mathcal{A}_{\tau_1} \phi(t-\tau_1) + \mathcal{A}_{\tau_2} \phi(t-\tau_2) + \mathcal{A}_{\tau_1\tau_2} \phi(t-\tau_1-\tau_2) \\ + \mathcal{B}_{\tau_h} r(t-\tau_h), \tag{3.15}$$

where $n = n_h + n_m + n_c + n_s$. $\mathcal{A}_0$, $\mathcal{A}_{\tau_h}$, $\mathcal{A}_{\tau_1}$, $\mathcal{A}_{\tau_2}$, $\mathcal{A}_{\tau_1\tau_2} \in \mathbb{R}^{n\times n}$, and $\mathcal{B}_{\tau_h} \in \mathbb{R}^{n\times n_h}$ are augmented system matrices defined as

$$\mathcal{A}_0 \triangleq \begin{bmatrix} A_h & \vec{0} & \vec{0} & \vec{0} \\ B_m C_h & A_m & \vec{0} & \vec{0} \\ \vec{0} & A_c - BcG_0C_s & \vec{0} & -B_c G_0 C_s \\ \vec{0} & \vec{0} & B_s C_c & A_s - B_s D_c G_0 C_s \end{bmatrix}, \tag{3.16}$$

$$\mathcal{A}_{\tau_h} \triangleq \begin{bmatrix} \vec{0} & -B_h C_m & \vec{0} & \vec{0} \\ \vec{0} & -B_m D_h C_m & \vec{0} & \vec{0} \\ \vec{0} & \vec{0} & \vec{0} & \vec{0} \\ \vec{0} & \vec{0} & \vec{0} & \vec{0} \end{bmatrix}, \tag{3.17}$$

$$\mathcal{A}_{\tau_1} \triangleq \begin{bmatrix} \vec{0} & \vec{0} & \vec{0} & \vec{0} \\ \vec{0} & \vec{0} & \vec{0} & \vec{0} \\ \vec{0} & B_c G_0 C_m & \vec{0} & \vec{0} \\ \vec{0} & B_s D_c G_0 C_m & \vec{0} & \vec{0} \end{bmatrix}, \tag{3.18}$$

$$\mathcal{A}_{\tau_2} \triangleq \begin{bmatrix} \vec{0} & \vec{0} & \vec{0} & \vec{0} \\ \vec{0} & \vec{0} & -B_m C_c & B_m D_c G_0 C_s \\ \vec{0} & \vec{0} & \vec{0} & \vec{0} \\ \vec{0} & \vec{0} & \vec{0} & \vec{0} \end{bmatrix}, \tag{3.19}$$

$$\mathcal{A}_{\tau_1\tau_2} \triangleq \begin{bmatrix} \vec{0} & \vec{0} & \vec{0} & \vec{0} \\ \vec{0} & -B_m D_c G_0 C_m & \vec{0} & \vec{0} \\ \vec{0} & \vec{0} & \vec{0} & \vec{0} \\ \vec{0} & \vec{0} & \vec{0} & \vec{0} \end{bmatrix}, \tag{3.20}$$

$$\mathcal{B}_{\tau_h} \triangleq \begin{bmatrix} B_h \\ B_m D_h \\ \vec{0} \\ \vec{0} \end{bmatrix}. \tag{3.21}$$

Assuming identical time-delays in the back and forth communication, $\tau_1 = \tau_2 = \tau_c$ holds, then the following state space representation follows

$$\dot{\phi}(t) = \mathcal{A}_0\phi(t) + \mathcal{A}_{\tau_h}\phi(t-\tau_h) + \mathcal{A}_{\tau_c}\phi(t-\tau_c) + \mathcal{A}_{\tau_c\tau_c}\phi(t-2\tau_c) + \mathcal{B}_{\tau_h}r(t-\tau_h), \tag{3.22}$$

where $\mathcal{A}_{\tau_c} \triangleq \mathcal{A}_{\tau_1} + \mathcal{A}_{\tau_2}$ and $\mathcal{A}_{\tau_c\tau_c} \triangleq \mathcal{A}_{\tau_1\tau_2}$. Characteristic equation of (3.22) is given by

$$CE = \det(sI - \mathcal{A}_0 - \mathcal{A}_{\tau_h}e^{-\tau_h s} - \mathcal{A}_{\tau_c}e^{-\tau_c s} - \mathcal{A}_{\tau_c\tau_c}e^{-2\tau_c s}) = 0. \tag{3.23}$$

which, when expanded, follows the general form

$$CE = \sum_{k=0}^{n}\sum_{j=0}^{n-k}\sum_{l=0}^{n-k-j} a_{kjl}(s)e^{-(k\tau_h+(j+2l)\tau_c)s}, \tag{3.24}$$

where $a_{kjl}(s)$ are polynomials in "s". Next, the *Rekasius substitution* is utilized[1]

$$e^{-\tau_j s} = \frac{1-T_j s}{1+T_j s},\ T_j \in \mathbb{R},\ j = h, c, \tag{3.25}$$

---

[1] Note that this substitution for single delay systems was proposed in [92], its extensions to multiple delays as well as developments in the single delay case can be found in [52].

which is an exact substitution for $s = j\omega_c$ roots of the characteristic equation. Then, a polynomial in T_j is obtained, which is given as

$$CE = \sum_{k=0}^{n} \sum_{j=0}^{n-k} \sum_{l=0}^{n-k-j} a_{kjl}(s) \left(\frac{1 - T_h s}{1 + T_h s} \right)^{k} \left(\frac{1 - T_c s}{1 + T_c s} \right)^{j+2l} . \tag{3.26}$$

Furthermore, (3.26) can be simplified by expanding it by $(1 + T_h s)^n (1 + T_c s)^{n-k}$, which does not bring any artificial $s = j\omega_c$ roots, since T_c and T_h are both real. Next, it can be shown that using the phase condition in (3.25), the following mapping between T_j and τ_j values holds:

$$\tau_j = \frac{2}{\omega_c} \left[\tan^{-1}(\omega_c T_j + k\pi) \right], \; k = 0, 1, \ldots ; j = h, c. \tag{3.27}$$

It is important to note that $s = j\omega_c$ roots of (3.23) and (3.26) one to one match [52] [51]. Since the transformed characteristic equation is provided in the polynomial form in (3.26), which is simpler than (3.23), all the imaginary axis crossings $s = j\omega_c$ are first calculated in terms of $T_c \in \mathbb{R}$ and $T_h \in \mathbb{R}$ from (3.26), for example, using Routh's array. Using these T_c and T_h values obtained from Routh's array, (3.27) can then be used to calculate the delays τ_j for which (3.23) has crossings at the same crossing $s = j\omega_c$.

Note that there are infinitely many delays corresponding to each pair (T_c, ω_c) and (T_h, ω_c) due to the counter k. The smallest positive of the delays and the corresponding imaginary axis crossings $\omega_c \in \Omega$ construct the so-called *"kernel curves"*, and the remaining positive delays construct the so-called *"offspring curves"*. In this problem, offspring curves follow the corresponding kernel curve in terms of stabilizing or destabilizing behavior of the root $s = j\omega_c$, which is associated with the property called *"Root Tendency (RT) invariance"*. *RT* for the specific problem at hand is calculated for $s = j\omega_c$ using

$$RT|_{s=\omega_c i}^{\tau_c} = sgn\{Im\,[H(s, \tau_h)]\}, \tag{3.28}$$

where

$$H(s, \tau_h) \quad = \quad \frac{\sum_{k=0}^{n} \sum_{j=0}^{n-k} \sum_{l=0}^{n-k-j} ((\frac{da_{kjl}(s)}{ds})_{kjl} - (2l + j)\tau_c a_{kjl})}{\sum_{k=0}^{n} \sum_{j=0}^{n-k} \sum_{l=0}^{n-k-j} (-a_{kjl} k)}. \tag{3.29}$$

In order to check the stability of a region on the plane of delays, one keeps τ_c fixed and uses the invariance property of RT with respect to time-delay τ_h to determine the number of unstable roots of the system on $\tau_c - \tau_h$, see details in the above-cited references.

3.1.2 Configuration 1

3.1.2.1 System Analysis

Figure 3.1 also depicts a human-in-the-loop telerobotic system with controller in effect. In this configuration, compared to the baseline, the environment effects (disturbances) are included, which means that the slave system touches an obstacle, say a tissue. Also, a master-side controller is considered to obtain force convergence. Therefore, the master-side controller dynamics is given as

$$\dot{x}_{cm}(t) = A_{cm}x_{cm}(t) + B_{cm}F_m(t), \quad x_{cm}(0) = 0 \tag{3.30}$$

$$F_{cm}(t) = C_{cm}x_{cm}(t) + D_{cm}F_m(t), \tag{3.31}$$

where $x_{cm}(t) \in \mathbb{R}^{n_{cm}}$ is the master side controller state vector, and $A_{cm} \in \mathbb{R}^{n_{cm}\times n_{cm}}$, $B_{cm} \in \mathbb{R}^{n_{cm}\times n_{F_m}}$, $C_{cm} \in \mathbb{R}^{n_{F_{cm}}\times n_{cm}}$, and $D_{cm} \in \mathbb{R}^{n_{F_{cm}}\times n_{F_m}}$ are the master side controller system matrices. Here, $F_m(t) \in \mathbb{R}^{n_{F_h}}$ is the force input applied to the master-side controller, and is defined similar to (3.14).

The slave robot dynamics is given by:

$$\dot{x}_s(t) = A_s x_s(t) + B_s(F_{cs}(t) + D), \quad x_s(0) = 0 \tag{3.32}$$

$$y_s(t) = C_s x_s(t) + D_s(F_{cs}(t) + D), \tag{3.33}$$

where $x_s(t) \in \mathbb{R}^{n_s}$ is the slave robot state vector, $y_s(t) \in \mathbb{R}^{n_{y_s}}$ is the output of the slave robot, and $A_s \in \mathbb{R}^{n_s\times n_s}$, $B_s \in \mathbb{R}^{n_s\times n_{F_c}}$, $C_s \in \mathbb{R}^{n_{y_s}\times n_s}$, and $D_s \in \mathbb{R}^{n_{y_s}\times n_{F_c}}$ are the slave robot system matrices, and $\tau_2 \in \mathbb{R}^+$ is the feedback communication time-delay. Moreover, the environment effect D is considered as disturbance with the dynamics given by $D = -W^T\sigma$, where W is the weight vector defined as $[k_e; B_e]$, and σ is a known basis function defined as $[x_s; \dot{x}_s]$. Hence, k_e and

B_e are respectively stiffness and damping coefficients of the environment model. Finally, the slave side controller is formulated in view of (3.9) and (3.10).

3.1.2.2 Stability Analysis

$\theta_1(t)$ and $\theta_2(t)$ are defined similar to (3.12) and (3.13). Moreover, using the incorporated disturbance model, it can be written that

$$D = G_1(-k_e - B_e A_s)x_s + G_1(-B_e B_s)F_{cs}, \tag{3.34}$$

where the existence of $G_1 = (I + B_e B_s)^{-1}$ is assumed implicitly. Now, considering (3.2), (3.6), and (3.9), it can be written that

$$F_m(t) = C_h x_h(t) + D_h \theta_1(t-\tau_h) - C_c x_c(t-\tau_2) - D_c \theta_2(t-\tau_2). \tag{3.35}$$

Finally, by using the previously defined $\phi(t)$, and using (3.4), (3.9), (3.12), (3.13), (3.32), and (3.35), the augmented state space representation of the dynamics is obtained as

$$\begin{aligned}\dot{\phi}^{cf_1}(t) = \mathcal{A}_0^{cf_1}\phi^{cf_1}(t) + \mathcal{A}_{\tau_h}^{cf_1}\phi^{cf_1}(t-\tau_h) + \mathcal{A}_{\tau_1}^{cf_1}\phi^{cf_1}(t-\tau_1) + \mathcal{A}_{\tau_2}^{cf_1}\phi^{cf_1}(t-\tau_2)\\ + \mathcal{A}_{\tau_1\tau_2}^{cf_1}\phi^{cf_1}(t-\tau_1-\tau_2) + \mathcal{B}_{\tau_h}^{cf_1} r(t-\tau_h),\end{aligned} \tag{3.36}$$

where $\mathcal{A}_0^{cf_1}$, $\mathcal{A}_{\tau_h}^{cf_1}$, $\mathcal{A}_{\tau_1}^{cf_1}$, $\mathcal{A}_{\tau_2}^{cf_1}$, $\mathcal{A}_{\tau_1\tau_2}^{cf_1} \in \mathbb{R}^{n\times n}$, and $\mathcal{B}_{\tau_h}^{cf_1} \in \mathbb{R}^{n\times n_h}$ are augmented system matrices. To be consistent with the previous case, $\tau_c = \tau_1 = \tau_2$ is assumed, as the communication time-delay while human operator reaction time-delay τ_h is in general different from τ_c, i.e., $\tau_h \neq \tau_c$. This then leads to the following state space representation

$$\begin{aligned}\dot{\phi}^{cf_1}(t) = \mathcal{A}_0^{cf_1}\phi^{cf_1}(t) + \mathcal{A}_{\tau_h}^{cf_1}\phi^{cf_1}(t-\tau_h) + \mathcal{A}_{\tau_c}^{cf_1}\phi^{cf_1}(t-\tau_c) + \mathcal{A}_{\tau_c\tau_c}^{cf_1}\phi^{cf_1}(t-2\tau_c) +\\ \mathcal{B}_{\tau_h}^{cf_1} r(t-\tau_h),\end{aligned} \tag{3.37}$$

where $\mathcal{A}_{\tau_c}^{cf_1} \triangleq \mathcal{A}_{\tau_1}^{cf_1} + \mathcal{A}_{\tau_2}^{cf_1}$ and $\mathcal{A}_{\tau_c\tau_c}^{cf_1} \triangleq \mathcal{A}_{\tau_1\tau_2}^{cf_1}$. The dynamics (3.37) is a linear time-invariant multiple-time-delay system, similar to (3.22), and its stability characteristics for various time-delay values can be investigated using the same method summarized in Section 3.1.1.2.

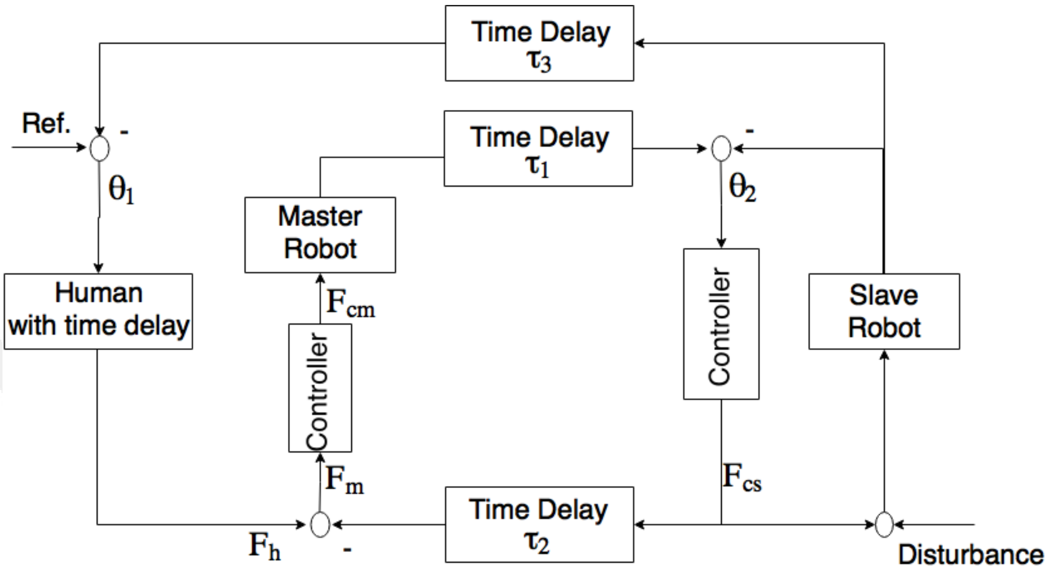

Figure 3.2: Block Diagram of the overall human-in-the-loop configuration 2 telerobotic system

3.1.3 Configuration 2

3.1.3.1 System Analysis

Human-in-the-loop telerobotics system with the block diagram depicted in Figure 3.2 is considered. In this set-up, compared to the baseline and configuration 1, see Figure 3.1, a visual feedback signal, that the human operator receives, is also considered. This is considered to represent a more practical scenario. Therefore, the input to the human dynamics is given by

$$\theta_1 \triangleq r(t) - y_s(t - \tau_3), \tag{3.38}$$

where $\theta_1(t) \in \mathbb{R}^{n_r}$ is the error vector with $r(t) \in \mathbb{R}^{n_r}$ defined as the reference input, and $y_s(t - \tau_3)$ as the delayed output of the slave robot. The rest of the dynamics is the same as that of the previous configurations.

3.1.3.2 Stability Analysis

Using the same approach in Section 3.1.1.2, along with (3.38), the previously defined $\phi(t)$, and Equations (3.4), (3.7), (3.9), (3.12), (3.13) and (3.14), the augmented state space representation of the dynamics is obtained as

$$\begin{aligned}\dot{\phi}^{cf_2}(t) &= \mathcal{A}_0^{cf_2}\phi^{cf_2}(t) + \mathcal{A}_{\tau_h}^{cf_2}\phi^{cf_2}(t-\tau_h) + \mathcal{A}_{\tau_1}^{cf_2}\phi^{cf_2}(t-\tau_1) + \mathcal{A}_{\tau_2}^{cf_2}\phi^{cf_2}(t-\tau_2)\\ &\quad + \mathcal{A}_{\tau_1\tau_2}^{cf_2}\phi^{cf_2}(t-\tau_1-\tau_2) + \mathcal{A}_{\tau_3\tau_h}^{cf_2}\phi^{cf_2}(t-\tau_h-\tau_3) + \mathcal{B}_{\tau_h}^{cf_2}r(t-\tau_h), \quad (3.39)\end{aligned}$$

where $\mathcal{A}_0^{cf_2}$, $\mathcal{A}_{\tau_h}^{cf_2}$, $\mathcal{A}_{\tau_1}^{cf_2}$, $\mathcal{A}_{\tau_2}^{cf_2}$, $\mathcal{A}_{\tau_1\tau_2}^{cf_2} \in \mathbb{R}^{n\times n}$, and $\mathcal{B}_{\tau_h}^{cf_2} \in \mathbb{R}^{n\times n_h}$ are augmented system matrices. Similarly, it is assumed that communication time-delays in both directions are identical, for consistency with respect to previous cases, $\tau_1 = \tau_2 = \tau_3 = \tau_c$. This then leads to the following state space representation

$$\begin{aligned}\dot{\phi}^{cf_2}(t) &= \mathcal{A}_0^{cf_2}\phi^{cf_2}(t) + \mathcal{A}_{\tau_h}^{cf_2}\phi^{cf_2}(t-\tau_h) + \mathcal{A}_{\tau_c}^{cf_2}\phi^{cf_2}(t-\tau_c) + \mathcal{A}_{\tau_c\tau_c}^{cf_2}\phi^{cf_2}(t-2\tau_c)\\ &\quad + \mathcal{A}_{\tau_c\tau_h}^{cf_2}\phi^{cf_2}(t-\tau_c-\tau_h) + \mathcal{A}_{\tau_c\tau_c\tau_h}^{cf_2}\phi^{cf_2}(t-2\tau_c-\tau_h) + \mathcal{B}_{\tau_h}^{cf_2}r(t-\tau_h),\end{aligned} \tag{3.40}$$

where $\mathcal{A}_{\tau_c}^{cf_2} \triangleq \mathcal{A}_{\tau_1}^{cf_2} + \mathcal{A}_{\tau_2}^{cf_2}$, $\mathcal{A}_{\tau_c\tau_c}^{cf_2} \triangleq \mathcal{A}_{\tau_1\tau_2}^{cf_2}$, $\mathcal{A}_{\tau_c\tau_h}^{cf_2} \triangleq \mathcal{A}_{\tau_3\tau_h}^{cf_2}$, $\mathcal{A}_{\tau_c\tau_c\tau_h}^{cf_2} \triangleq \mathcal{A}_{\tau_1\tau_3\tau_h}^{cf_2}$. The dynamics (3.40) is a linear time-invariant multiple-time-delay system, similar to (3.22), and its stability characteristics for various time-delay values can be investigated using the same method summarized in Section 3.1.1.2.

3.2 Results and Discussions

3.2.1 Preliminaries

For the telerobotic system architectures introduced above, a PI controller at the slave side is considered in order to synchronize the master and slave robots' velocities. When applicable, depending on the configuration, the controller at the master side is also a PI controller.

Moreover, a Neal-Schmidt Model [4] is considered to capture human operator's dynamics given by $G_h = k_p\frac{\alpha s+1}{\beta s+1}e^{-\tau_h s}$, where $k_p \in \mathbb{R}^+$ is the human operator's

Table 3.1: Numerical data used in all scenarios

Human model gain (k_p)	1 $[Nsec/m]$
Human time constant (α)	10 $[sec]$
Human time constant (β)	1 $[sec]$
Slave-side controller proportional gain (B_{cs})	5 $[Nsec/m]$
Slave-side controller integral gain (K_{cs})	10 $[N/m]$
Master-side controller proportional gain (B_{cm})	0.1 $[Nsec/m]$
Master-side controller integral gain (K_{cm})	0.2 $[N/m]$
Master and salve robot mass (m_m and m_s)	1 $[kg]$
Stiffness of the environment model (k_e)	0.1 $[N/m]$
Damping of the environment model (B_e)	0.2 $[Nsec/m]$

gain, $\alpha \in \mathbb{R}^+$ and $\beta \in \mathbb{R}^+$ are time constants, and $\tau_h \in \mathbb{R}^+$ is the human operator reaction time-delay.

The master and slave robot dynamics are given as

$$m_m \dot{v}_m(t) = F_{cm}, \quad v_m(0) = 0, \tag{3.41}$$

$$m_s \dot{v}_s(t) = F_{cs} + D, \quad v_s(0) = 0, \tag{3.42}$$

where $v_m(t) = \dot{x}_m(t) \in \mathbb{R}$ and $v_s(t) = \dot{x}_s(t) \in \mathbb{R}$. Therefore, master and slave robots transfer functions are given by $G_m = \frac{1}{m_m s}$ and $G_s = \frac{1}{m_s s}$. The slave- and master-side PI controllers dynamics are given by $\frac{B_{cs}s+K_{cs}}{s}$ and $G_{cm} = \frac{B_{cm}s+K_{cm}}{s}$, respectively, where B_{cs}, K_{cs}, B_{cm}, $K_{cm} \in \mathbb{R}^+$ are the associated controller parameters.

Numerical values of the parameters used in all the scenarios are provided in Table 3.1.

3.2.2 Stability Analysis of the Baseline Configuration

For the baseline telerobotic configuration depicted in Figure 3.1, the complete stability picture is provided in Figure 3.3 for a range of time-delays. Note that the gray area marks the stable region, and red and blue curves, which correspond to kernel and offspring curves, respectively, construct the boundaries where the

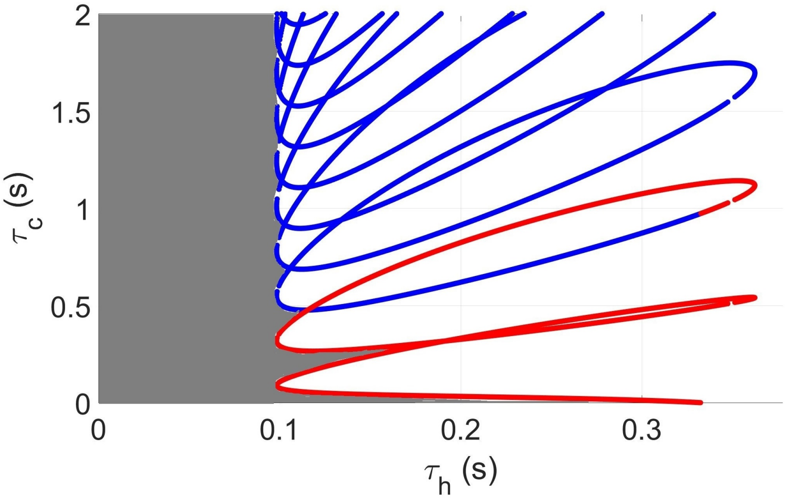

Figure 3.3: Stability characterization of the baseline architecture of the human-in-the-loop telerobotic system in terms of the communication time-delay τ_c and the human operator reaction time-delay τ_h. Red line is the *kernel curve*, and blue lines are the *offspring curves*. Gray shaded region shows the stable areas.

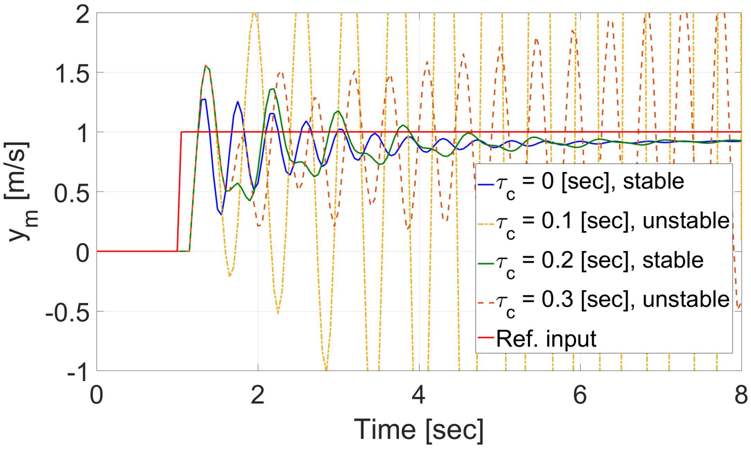

Figure 3.4: Output of the master system in the baseline configuration for the case of $\tau_h = 0.15$s and four different τ_c values for which the stable-unstable-stable-unstable transition is observed.

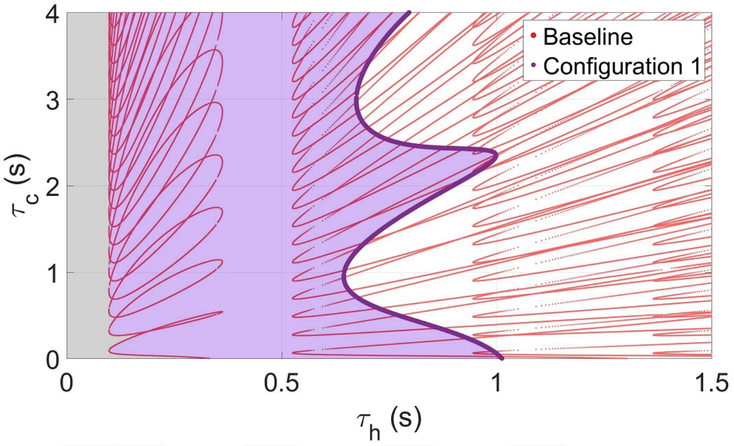

Figure 3.5: Comparison of stability characterization of the human-in-the-loop configuration 1 telerobotic system in terms of communication τ_c and human operator reaction time-delays τ_h with respect to the baseline. Light purple area marks the stable region gained by utilizing this configuration, which is beyond the gray area obtained in Figure 3.3 in the baseline configuration and is stable in configuration 1 as well.

system has at least one imaginary pole at $s = j\omega$. It is noted that the area where the human reaction time-delay is less than 0.1 seconds indicates a stable region regardless of the communication time-delay τ_c showing that τ_c may not be the main concern for stability. Determining factor is rather the human operator reaction time-delay, which causes instability even at very small values compared to what the actual human operator reaction time-delays might be (for example 0.3 seconds in [4]) for a given τ_c. Therefore, this baseline architecture may not be feasible and can easily lead to instability for the considered system characteristics. Figure 3.4 depicts the output of the master for the baseline configuration at different communication time-delay values. The results are in agreement with the stability picture provided in Figure 3.3.

3.2.3 Stability Analysis of Configuration 1

Figure 3.5 shows how stability limits change with the consideration of environment effects and master-side controller. Note that the red lines depict the kernel

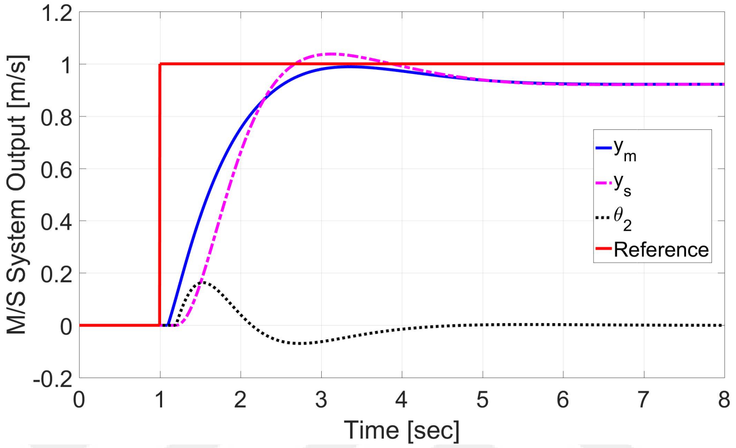

Figure 3.6: The synchronization of the master (y_m) and slave (y_s) outputs, together with the reference trajectory, for configuration 1, provided in Figure 3.1, for $\tau_c = 0.1$ [sec] and $\tau_h = 0.8$ [sec]. The synchronization error (θ_2) converges to zero.

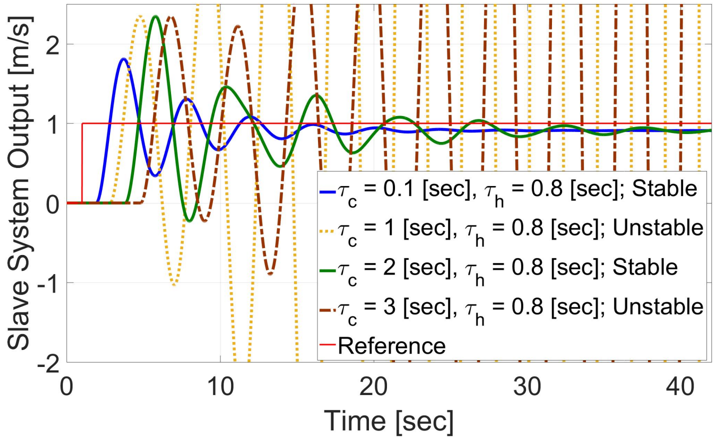

Figure 3.7: The response of configuration 1 presenting the stable-to-unstable and unstable-to-stable transitions as τ_c increases, for a fixed τ_h.

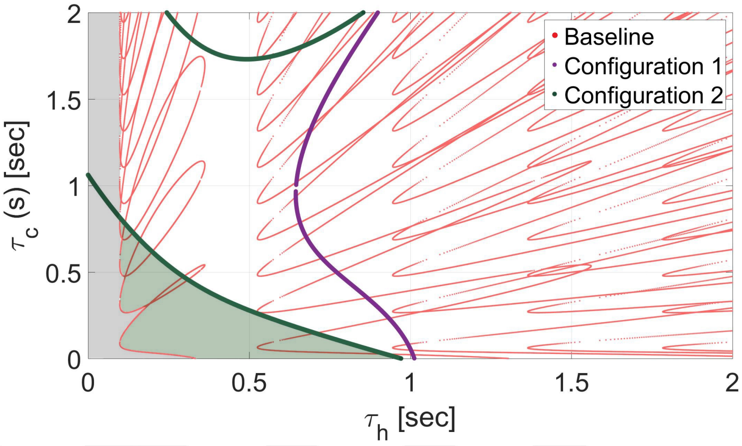

Figure 3.8: Comparison of stability characterization of the configuration 2 in terms of communication τ_c and human operator reaction time-delays τ_h with respect to the baseline and configuration 1. The green area marks the stable region added to that in baseline but with a loss of gray stable regions above the green boundary (originally stable in the baseline architecture).

and offspring curves of the baseline system a part of which was provided in Figure 3.3, and the thick purple curve depicts those of the configuration 1, where the region on the left of this curve shows the stable region (light purple and gray shaded areas). It can be seen that configuration 1 can accommodate much larger human operator reaction time-delays τ_h.

Next, a set of simulations is performed. Figure 3.6 depicts system output for the master and slave systems. Figure 3.7 shows the response of the slave robot to a step reference input for a range of time-delay values. Note the transition from stability to instability and vice versa for a single value of human operator reaction time-delay, $\tau_h = 0.8s$, which is in agreement with the stability picture given in Figure 3.5.

3.2.4 Stability Analysis of Configuration 2

Figure 3.8 shows how the visual feedback affects the stability of the closed loop system compared to that of the baseline and configuration 1 systems. Note that

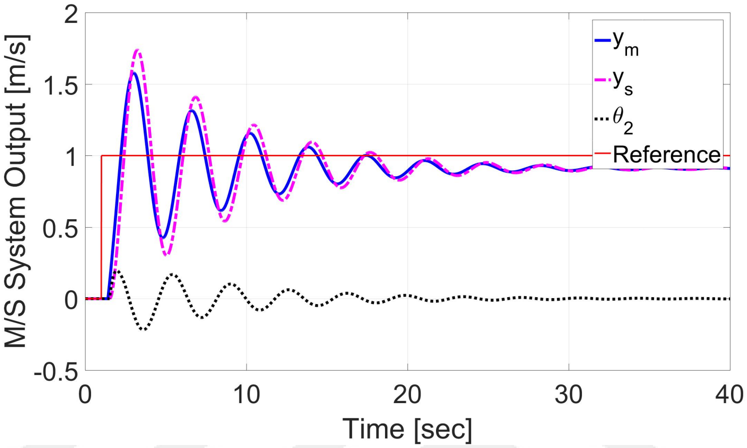

Figure 3.9: Master and slave systems output, and θ_2 signals of the human-in-the-loop configuration 2 telerobotic system for $\tau_c = 0.1$ and $\tau_h = 0.4$ seconds.

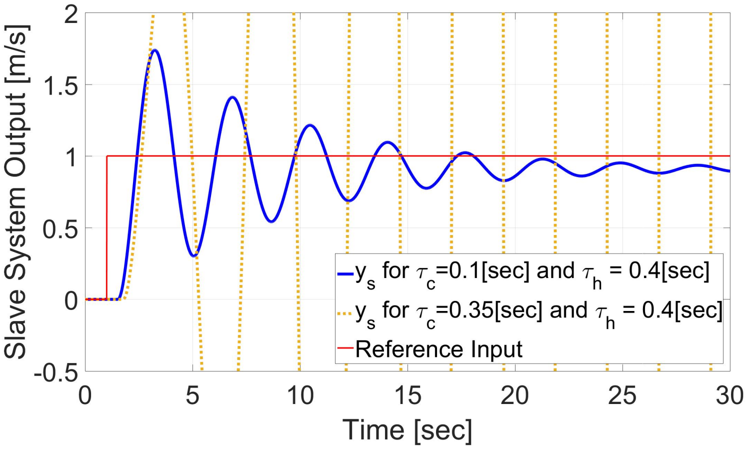

Figure 3.10: Response of configuration 2 showing the stable-to-unstable transition for different τ_c values given a fixed value of τ_h.

the dark green curves depict the kernel and offspring curves for this configuration, and the light shaded green region indicates the stability region added to that in the baseline architecture. Although this configuration can accommodate considerably larger human operator reaction time-delays (area below the green boundary) compared to the baseline, one can see how limited the stability region becomes, compared to configuration 1, especially along τ_c axis.

Figure 3.9 depicts the outputs of the master and slave systems for $\tau_c = 0.1$ and $\tau_h = 0.4$ seconds. Figure 3.10 shows stable to unstable transition for increasing values of τ_c. It is noted that a stable-unstable-stable transition is not observed for configuration 2, which means that stability cannot be recovered for larger delays once the system enters the unstable zone in the delay parameter space.

Chapter 4

Control-Oriented Mathematical Modeling of the Geomagic® Touch™ (PHANToM® Omni®)

In this chapter, a data driven and first principles modeling of the Geomagic® Touch™ (formerly PHANToM® Omni®) device is considered. A simple linear model is provided for one of the degrees of freedom based on fundamental insights into the device structure and in light of experimental observations. The parameters of the model are estimated through extensive tests.

4.1 Device Dynamics

Fig. 4.1 shows the Geomagic® Touch™ (formerly PHANToM® Omni®), a schematic of which is shown in Fig. 4.2. In this device, in order to prevent backlash, a preloaded tendon cable is used whose length is adjusted by a setscrew [93]. Moreover, as shown in Figs. 4.3-4.6, the arm, whose moment of inertia will be

---

* Readily available at *www.hizook.com/blog/2012/04/22/two-more-robotics-companies-get-acquired-my-robot-nation-and-sensable-technologies*. Permission to use these figures is pending.

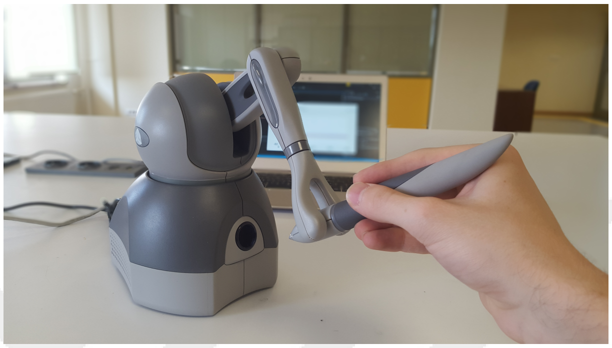

Figure 4.1: Geomagic® Touch™ (formerly, PHANToM® Omni®) device.

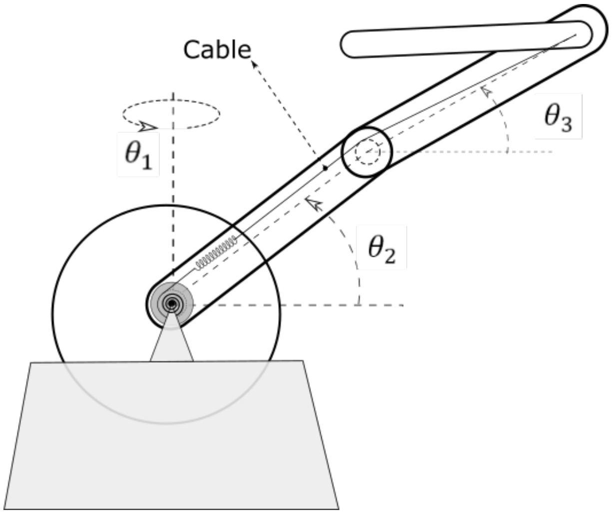

Figure 4.2: A schematic of Geomagic® Touch™ (formerly, PHANToM® Omni®) device.

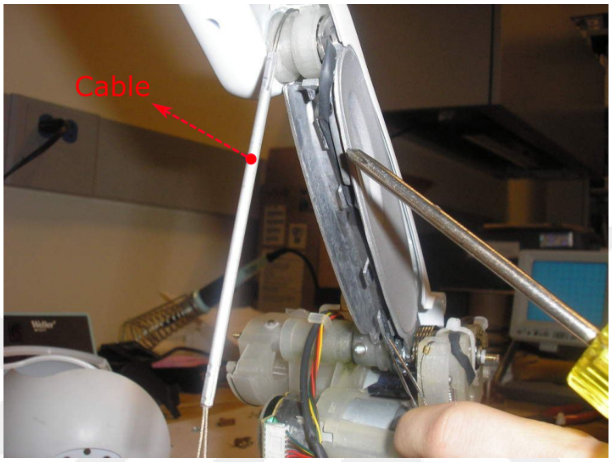

Figure 4.3: Internal parts of the Geomagic® Touch™ (formerly PHANToM® Omni®) device*: cable.

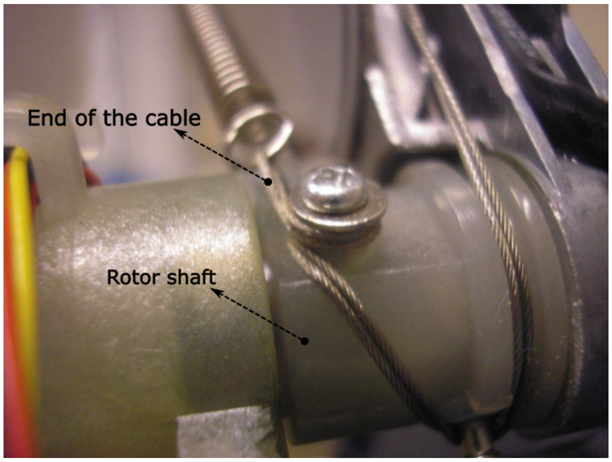

Figure 4.4: Internal parts of the Geomagic® Touch™ (formerly PHANToM® Omni®) device*: connection of the cable and the rotor shaft.

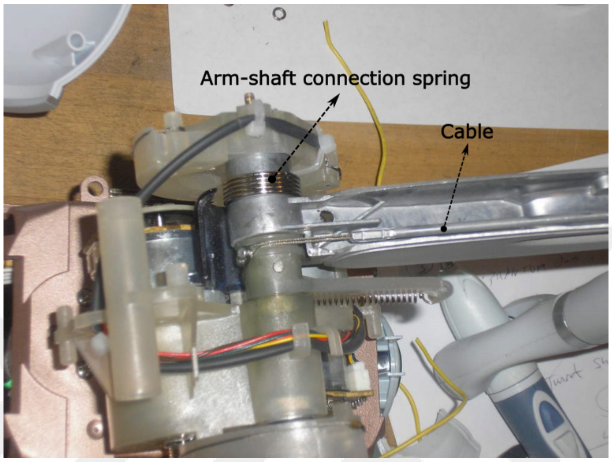

Figure 4.5: Internal parts of the Geomagic® Touch™ (formerly PHANToM® Omni®) device*: connection of the arm and rotor shaft.

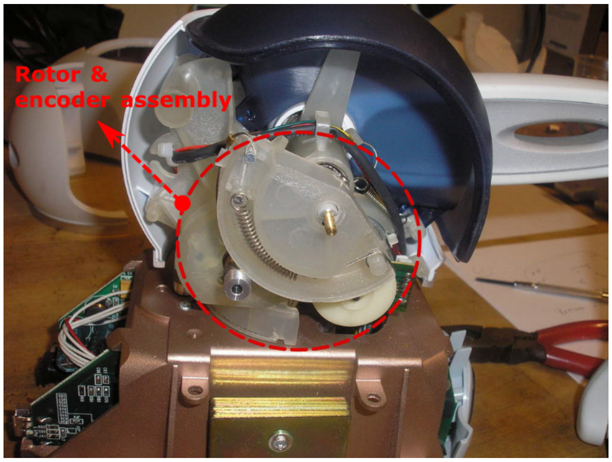

Figure 4.6: Internal parts of the Geomagic® Touch™ (formerly PHANToM® Omni®) device*: the actuator and encoder connection.

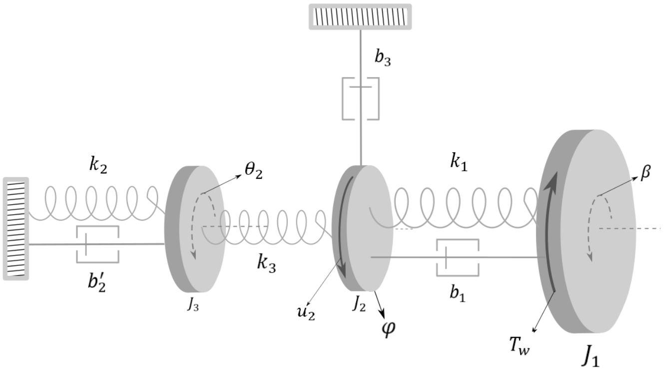

Figure 4.7: Schematic showing the system elements and their connections for the Geomagic® Touch™ (formerly PHANToM® Omni®) device while all degrees of freedom are constrained except θ_2.

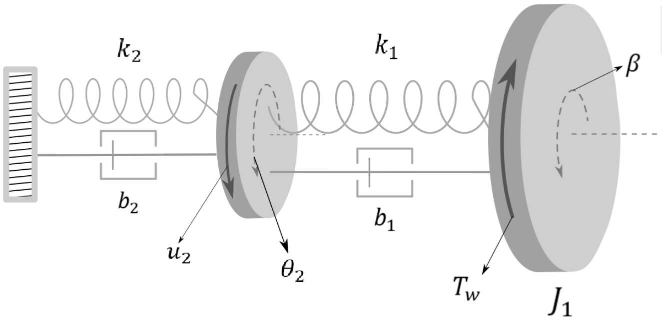

Figure 4.8: Interim schematic showing the system elements and their connections for the Geomagic® Touch™ (formerly PHANToM® Omni®) device.

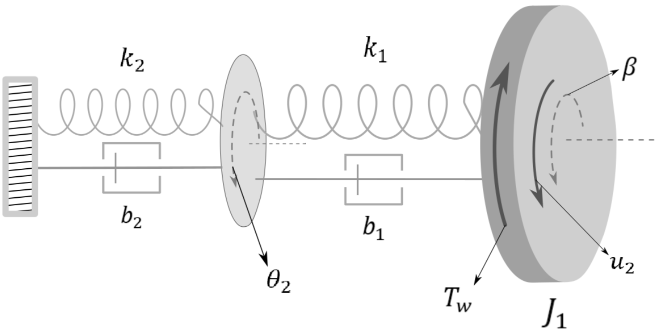

Figure 4.9: Simplified Schematic showing the system elements and their connections for the Geomagic® Touch™ (formerly PHANToM® Omni®) device.

called as J_1, is connected to the rotor shaft, whose moment of inertia will be called as J_2, by torsional spring, the stiffness of which will be represented by k_1. A damping element with a coefficient b_1, representative of possible viscous friction at the arm-rotor connection, is also considered (see Fig. 4.7). The rotor shaft also experiences a resisting damping force, with a coefficient of b_3, due to the back-EMF effect [94]. The rotor shaft is connected to the encoder using a stiff spring k_3. The encoder assembly, whose inertia is given as J_3, is assumed to be experiencing a spring-damper effect with coefficients k_2 and $b_2^{'}$, respectively. Since the spring k_3 is thought to be relatively stiff to minimize measurement errors, it is assumed that its deflection is negligible, which helps simplify the structure given in Fig. 4.7 and obtain the configuration given in Fig. 4.8, where $b_2 = b_2^{'} + b_3$. Moreover, it is assumed that the springs, dampers, and the rotor are of negligible weight, which provides an even simpler structure given in Fig. 4.9, where there is only one inertia, J_1. The only degree of freedom of the main arm in our analysis is the movement along the pitch axis, which is represented by the change of angle β. The remaining degrees of freedom of the device, i.e., the motions around the roll and yaw axes, are assumed to be constrained.

Under the above assumptions, the differential equation representing the dynamics of the device is given by

$$J_1 \frac{d^2\beta(t)}{dt^2} = u_2 - T_w - k_1(\beta(t) - \theta_2(t)) - b_1(\frac{d\beta(t)}{dt} - \frac{d\theta_2(t)}{dt}), \tag{4.1}$$

where $u_2 \in \mathbb{R}$ and $T_w \in \mathbb{R}$ are the input to the device and gravitational torque, respectively. Since it is assumed that the inertia of the rotor is much smaller than that of the main arm, the forces acting through the spring-damper blocks ($b1 - k1$, $b2 - k2$) can be taken as equal:

$$k_1(\beta(t) - \theta_2(t)) + b_1(\frac{d\beta(t)}{dt} - \frac{d\theta_2(t)}{dt}) = k_2\theta_2(t) + b_2\frac{d\theta_2(t)}{dt}. \tag{4.2}$$

Taking the Laplace transform of (4.1) and (4.2) and equating the common terms yields the following transfer function between θ_2, the rotation measured by the device sensors, and the net input is obtained

$$G = \frac{\Theta_2(s)}{U_s(s)} = \frac{N(s)}{D(s)}, \tag{4.3}$$

where $N(s) = b_1 s + k_1$ and $D(s) = J_1(b_1 + b_2)s^3 + (J_1(k_1 + k_2) + b_1 b_2)s^2 + (b_1 k_2 + b_2 k_1)s + k_1 k_2$.

Considering the general governing third order dynamics of the device, which could be deduced from (4.3), it can be written

$$P_1 \frac{d^3\theta_2}{dt^3} + P_2 \frac{d^2\theta_2}{dt^2} + P_3 \frac{d\theta_2}{dt} + P_4 \theta_2 = u_2 + (b_1/k_1)\frac{du_2}{dt} + P_4 u_2 - T_w, \quad (4.4)$$

where $P_{1-4} \in \mathbb{R}$ could be easily evaluated compared to (4.3). When the device arm is freely released to reach its equilibrium point, $P_4 \theta_{2eq} = -T_w$, and therefore, $\theta_{2eq} = -T_w/P_4$. Defining $\bar{\theta}_2 = \theta_2 - \theta_{2eq}$, and substituting into (4.4), it can be obtained that

$$P_1 \frac{d^3\bar{\theta}_2}{dt^3} + P_2 \frac{d^2\bar{\theta}_2}{dt^2} + P_3 \frac{d\bar{\theta}_2}{dt} + P_4 \bar{\theta}_2 = u_2 + (b_1/k_1)\frac{du_2}{dt}. \quad (4.5)$$

Writing the initial condition of $\bar{\theta}_2$ as $\bar{\theta}_2(t = 0) = \bar{\theta}_{2,0}$, and defining $\alpha = \bar{\theta}_2 - \bar{\theta}_{2,0}$, it can be obtained that

$$P_1 \frac{d^3\alpha}{dt^3} + P_2 \frac{d^2\alpha}{dt^2} + P_3 \frac{d\alpha}{dt} + P_4 \alpha = u_2 + (b_1/k_1)\frac{du_2}{dt} - P_4 \bar{\theta}_{2,0}. \quad (4.6)$$

$P_4 \bar{\theta}_{2,0}$ can be obtained using (4.5) in a static test, in which a torque is gradually applied, the very first sign of motion is spotted, and the associated torque value is recorded. This value is found to be approximately 0.24 Nm. It is noted that the transfer function (4.3) is derived assuming zero initial conditions. This assumption is no longer needed by defining the input as $u_2 - 0.24$ and the output as α.

4.2 Parameter Estimation

4.2.1 Preliminaries

The experimental setup is given in Fig. 4.2. For parameter estimation, an upward step torque input is first exerted with different input amplitudes long enough for it to reach various steady state values, α_{ss}, scanning a range of about 2-23 degrees in the device workspace, and then, let the arm fall freely. These two stages are called upward and downward motions throughout this chapter. The position sensing/input is done using the x, y, z digital encoders of the device, which has resolution of ~ 0.055 millimeters according to the manufacturer. For the upward motion, using the step-response input/output data, a transfer function with three poles and one zero, similar to (4.3) is fitted using standard Matlab system identification toolbox using discrete time domain transfer function fitting with no preprocessing. Totally 7 tests were conducted for a range of inputs from $u_2 = 0.25$ [Nm] to $u_2 = 0.36$ [Nm]. A similar procedure is followed for the downward motion using the free fall data of the arm for a number of distinct initial angular deflections (totally 7 tests). Accordingly, an experimentally derived transfer function is obtained for each upward/downward test similar to the following

$$G_{exp} = \frac{a_0 s + a_1}{s^3 + a_2 s^2 + a_3 s + a_4}. \tag{4.7}$$

Using (4.3)-(4.7), it can be shown that the parameters of (4.3) represent the following physical quantities:

$$\begin{aligned} a_0 &= \frac{b_1}{J_1(b_1+b_2)}, && (4.8)\\ a_1 &= \frac{k_1}{J_1(b_1+b_2)}, && (4.9)\\ a_2 &= \frac{k_1+k_2}{b_1+b_2}, && (4.10)\\ a_3 &= \frac{b_1 k_2 + b_2 k_1}{J_1(b_1+b_2)}, && (4.11)\\ a_4 &= \frac{k_1 k_2}{J_1(b_1+b_2)}. && (4.12) \end{aligned}$$

In order to check the accuracy of the results, the relative error vector between the recorded experimental and the predicted trajectory vectors of the arm, α_{exp} and α_{th}, is used which is defined as

$$e_{rel} = \frac{||e||}{||\alpha_{exp}||}, \tag{4.13}$$

where $e = \alpha_{exp} - \alpha_{th}$.

---

[*] https://www.3dsystems.com/haptics-devices/touch/specifications

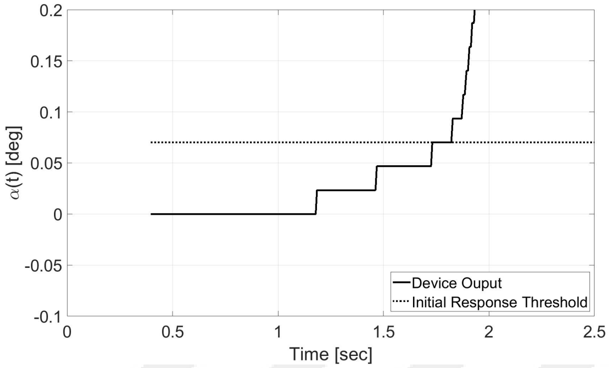

Figure 4.10: Very first moments of the response of the device with the considered threshold.

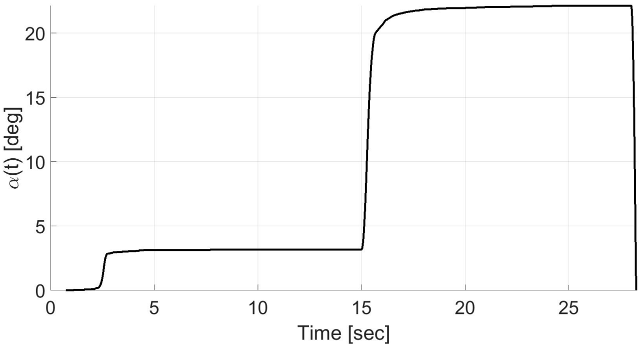

Figure 4.11: Test of successive step inputs.

4.2.2 A Discussion on the Technical Issues

In the experiments, a delay of about 0.4 seconds is experienced at the beginning of the device operation (device API build time) and a period of about 1 second of sedentariness while the clock is ticking (see Fig. 4.10). However, it is observed that this issue is not persistent after the initial device operation. In Fig. 4.11, two consecutive responses of the device to step inputs is shown. Although the problematic delay occurs in the first response, the device responds almost immediately in the second run at $t = 15$ seconds. Therefore, a delay term in the response is not taken into account and it is assumed that the initial response starts at $\alpha = 0.08$ degrees. This α threshold is shown in Fig. 4.10.

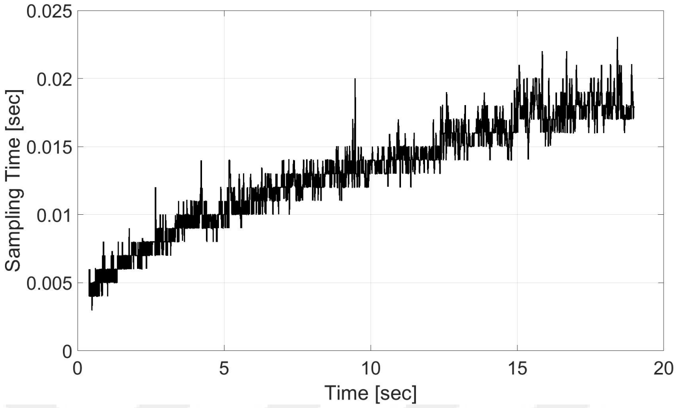

Figure 4.12: How sampling time changes over the course of a typical experiment. Same trend is observed in all experiments.

Table 4.1: Transfer functions of Fig. 4.13.

a	$\frac{6614}{s^3+3.548s^2+54.9s+52.69}$	b	$\frac{0.0009573s+5504}{s^3+4.667s^2+24.94s+32.27}$
c	$\frac{0.0005488s+6776}{s^3+5.284s^2+24.25s+39.86}$	d	$\frac{0.002028s+7242}{s^3+4.628s^2+26.67s+37.61}$
e	$\frac{0.001107s+8860}{s^3+5.569s^2+27.24s+46.76}$	f	$\frac{0.002731s+6619}{s^3+4.764s^2+21.92s+32.41}$
g	$\frac{0.00135s+8700}{s^3+5.631s^2+27.22s+46.99}$		

Another technical issue is that the sampling rate during the data acquisition is not constant during the experiments, it increases gradually from around 0.004 seconds at the beginning to around 0.02 seconds at the end, as revealed by Fig. 4.12, for a typical test. To obtain an evenly spaced (in-time) data, linear interpolation is deployed assuming an 0.004 seconds data collection interval T_s.

4.2.3 Transfer Functions Modeling the Upward Motion

Fig. 4.13 shows the output of each transfer function fitted to the data. Transfer functions are provided in Table. 4.1.

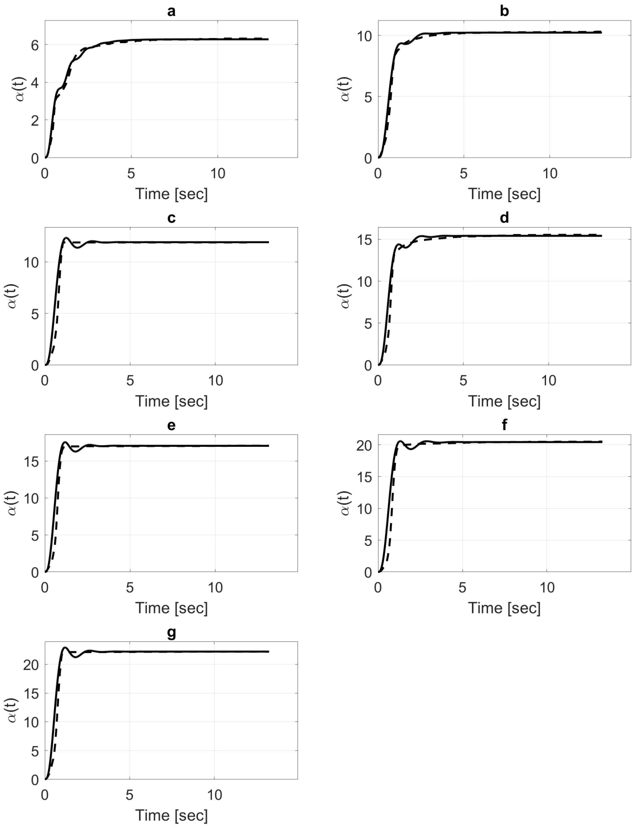

Figure 4.13: Output of each transfer function (solid curves) specific to each test data (dashed curves). The associated relative error of the data for the interval between $t = 0$ and $t = t_s$ (1% settling time), obtained using (4.13), are 0.0303 (a), 0.0426 (b), 0.1485 (c), 0.0611 (d), 0.1506 (e), 0.1062 (f), and 0.1383 (g).

,

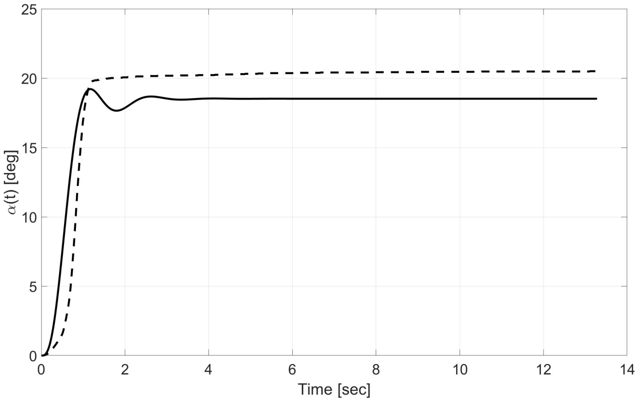

Figure 4.14: Output of (4.14) (solid curve) for a typical test data (dashed curve). The associated relative error of the data for the interval between $t = 0$ and $t = t_s$ (1% settling time), obtained using (4.13), is 0.1473.

Table 4.2: Transfer functions of Fig. 4.15.

a	$\frac{0.0008822s+2.466e6}{s^3+517.4s^2+1.704e4s+7.927e4}$	b	$\frac{6.134e{-}5s+2.45e6}{s^3+759.9s^2+7970s+4.663e4}$
c	$\frac{2.598e6}{s^3+594.5s^2+8686s+4.303e4}$	d	$\frac{5.034e{-}5s+3.114e6}{s^3+653.5s^2+8603s+2.334e4}$
e	$\frac{0.01295s+2.709e6}{s^3+674.5s^2+3135s+7495}$	f	$\frac{2.784e6}{s^3+461.9s^2+4894s+7485}$
g	$\frac{2.887e6}{s^3+544.6s^2+4055s+6711}$		

Next, an average transfer function of all those transfer function is provided as

$$G_{up} = \frac{0.001246s + 7188}{s^3 + 4.87s^2 + 29.59s + 41.23}. \tag{4.14}$$

Fig. 4.14 shows an example output of (4.14) for a typical test.

4.2.4 Transfer Functions Modeling the Downward Motion

In this section, transfer functions estimated using each and every downward motion test data are provided. Fig. 4.15 shows output of each of those transfer functions for each test data. The transfer functions used in these results are provided in Table 4.2. Similarly, an average transfer function of all those transfer

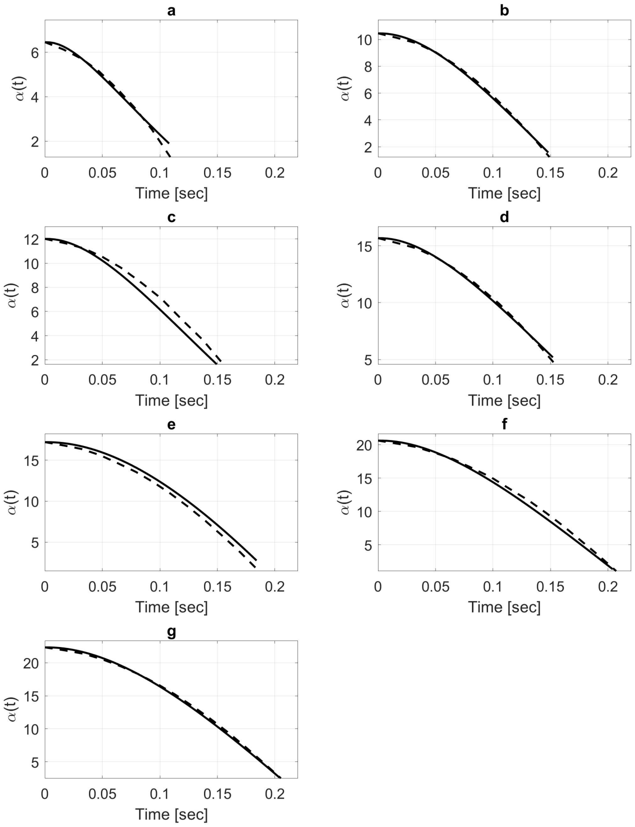

Figure 4.15: Output of each transfer function (solid curves) and the test data (dashed curves) estimated using downward data. The associated relative error of the data, obtained using (4.13), are 0.0360 (a), 0.0170 (b), 0.0742 (c), 0.0140 (d), 0.0498 (e), 0.0340 (f), and 0.0150 (g).

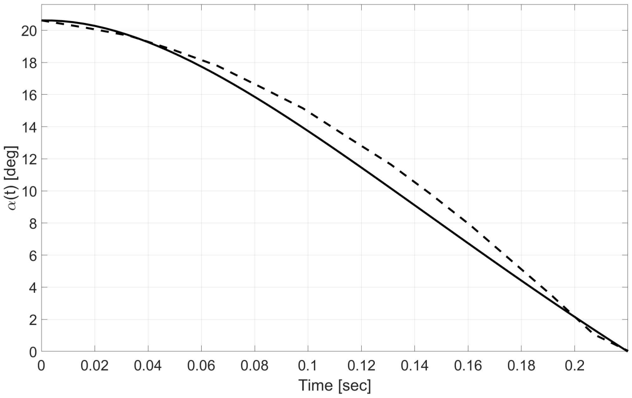

Figure 4.16: Output of (4.15) (solid curve) for a typical test data (dashed curve). The associated relative error of the data, obtained using (4.13), is 0.0288.

Table 4.3: Transfer functions of Fig. 4.17.

a	$\frac{3991s+1.177e04}{s^3+9.367s^2+97.13s+93.76}$	b	$\frac{4547s+1.172e04}{s^3+13.2s^2+52.37s+68.39}$
c	$\frac{3521s+1.089e04}{s^3+6.729s^2+33.94s+64.15}$	d	$\frac{1337s+1100}{s^3+4.785s^2+10.23s+5.725}$
e	$\frac{3541s+1.45e04}{s^3+7.185s^2+38.73s+76.6}$	f	$\frac{1713s+4417}{s^3+5.453s^2+16.13s+21.76}$
g	$\frac{3596s+1.389e04}{s^3+7.154s^2+37.97s+75.07}$		

function is provided as

$$G_{down} = \frac{0.001992s + 2.715e06}{s^3 + 600.9s^2 + 7769s + 3.056e04}. \tag{4.15}$$

Fig. 4.16 shows an example output of (4.15) for a typical test.

4.2.5 A single transfer function for the whole motion

To obtain a single transfer function for the whole motion, containing both upward and downward motions, a similar approach as in the previous subsections is followed; however, a transfer function is fitted to the both upward and downward motions data, i.e., the whole motion data. Fig. 4.17 shows the output of all

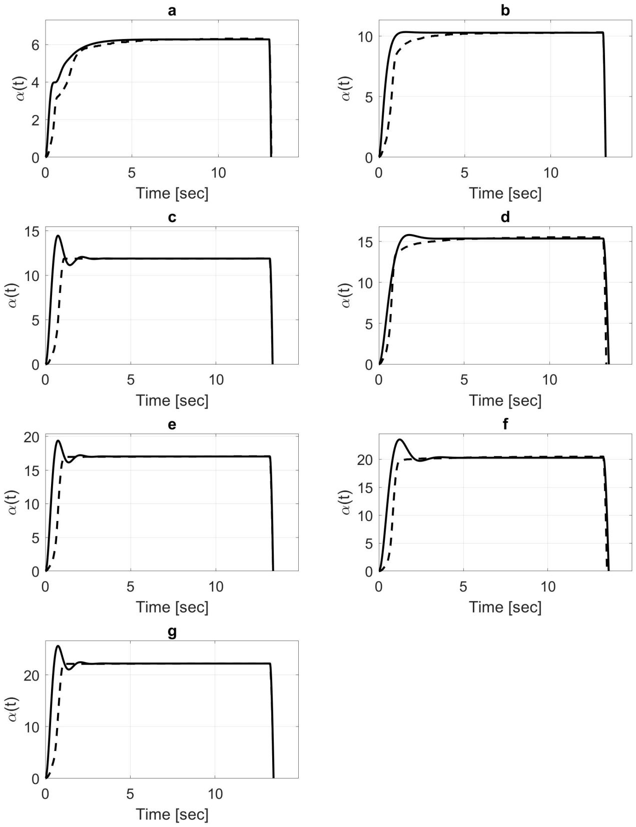

Figure 4.17: Output of each transfer function (solid curves) specific to each test data (dashed curves). The associated relative error of the data for the interval between $t = 0$ and $t = t_s$ (1% settling time), obtained using (4.13), are 0.1284 (a), 0.1910 (b), 0.5137 (c), 0.0863 (d), 0.5564 (e), 0.2212 (f), and 0.5497 (g).

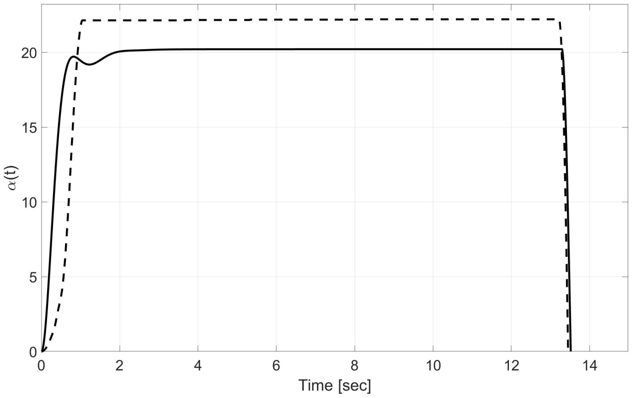

Figure 4.18: Output of (4.16) (solid curve) for a typical test data (dashed curve). The associated relative error of the data for the interval between $t = 0$ and $t = t_s$ (1% settling time), obtained using (4.13), is 0.3848.

transfer functions fitted to the individual experimental data, when the sampling rate is selected as 0.004. Associated transfer functions are provided in Table 4.3.

The average of those transfer functions, obtained at different operating regions, is calculated as

$$G = \frac{3178s + 9755}{s^3 + 7.697s^2 + 40.93s + 57.92}. \tag{4.16}$$

It is noted that the average transfer function is obtained by averaging the coefficients. An example response of (4.16) is given in Fig. 4.18.

Chapter 5

Conclusion and Future Work

With the recent developments in the systems architecture and design, and increasingly interlinked design of the systems where human operators are elements of the overall closed loop system, analyzing the interactions between human operators and the other system elements and design of effective schemes of such interactions are of crucial importance. In this thesis, two human-in-the-loop systems are analyzed from stability and performance points of view. In the first case, human-in-the-loop model reference adaptive control architectures are analyzed and fundamental stability limits are explicitly derived. Specifically, this stability limits result from the coupling between outer and inner loop architectures, where the outer loop portion includes the human dynamics modeled as a linear dynamical system with time delay and the inner loop portion includes the uncertain dynamical system, the reference model, the parameter adjustment mechanism, and the controller. It is shown that when the given set of human model and reference model parameters satisfy this stability limit, the closed-loop system trajectories are guaranteed to be stable. The theoretical stability predictions of the proposed approach were verified via several simulation studies. The effects of linear filtering on the human-in-the-loop model reference adaptive control architectures is also analyzed to study the stability and performance of the overall closed loop system in the presence of human reaction time delays. Specifically, the filter parameters are designed to stabilize the closed-loop, MRAC-human-filter dynamics. Moreover, a key transfer function between the MRAC error singnal and the human error signal (input signal to the human block) arising in the task execution was developed to study how MRAC and human model interact with each other. This study shows that the proposed filter is effective in suppressing undesirable oscillations, enabling a more effective and synergistic MRAC-human integration.

Telerobotic systems are analyzed in the other scenario. It is shown how the stability of a human-in-the-loop telerobotic system is affected by the communication architecture between the master and the slave sides. Considering the human operator with reaction time-delay as an element of the bilateral telerobotic system that naturally comes with communication time-delays, the stability of the closed-loop system with multiple time-delays is investigated via using rigorous stability analysis tools. The stability characteristics of three different telerobotic system architectures are provided, together with a discussion on the implementation challenges. In the final part of the thesis, the problem of modeling of PHANToM® Omni® haptic device, a relatively common device employed in haptics and teleoperations studies, is investigated. First principles modeling approach together with experimental observations resulted in linear models of the device. Deriving a more general model of the device is considered to be a future research direction.

Bibliography

[1] F. Lamnabhi-Lagarrigue, A. Annaswamy, S. Engell, A. Isaksson, P. Khargonekar, R. M. Murray, H. Nijmeijer, T. Samad, D. Tilbury, and P. V. den Hof, "Systems & Control for the future of humanity, research agenda: Current and future roles, impact and grand challenges," *Annual Reviews in Control*, vol. 43, pp. 1 – 64, 2017.

[2] D. Helbing, "Traffic and related self-driven many-particle systems," *Reviews of Modern Physics*, vol. 73, pp. 1067–1141, 2001.

[3] D. T. McRuer, "Mathematical models of human pilot behavior," Jan. 1974.

[4] D. K. Schmidt and B. J. Bacon, "An optimal control approach to pilot/vehicle analysis and the neal-smith criteria," *Journal of Guidance, Control, and Dynamics*, vol. 6, no. 5, pp. 339 – 347, 1983.

[5] A. J. Thurling, "Improving uav handling qualities using time delay compensation," tech. rep., DTIC Document, 2000.

[6] S. Ryu and D. Andrisani, "Longitudinal flying qualities prediction for nonlinear aircraft," *Journal of guidance, control, and dynamics*, vol. 26, no. 3, pp. 474–482, 2003.

[7] J. B. Witte, "An investigation relating longitudinal pilot-induced oscillation tendency rating to describing function predictions for rate-limited actuators," tech. rep., DTIC Document, 2004.

[8] C. J. Miller, "Nonlinear dynamic inversion baseline control law: Architecture and performance predictions," *AIAA Guidance, Navigation, and Control Conference*, 2011.

[9] M. Treiber, A. Kesting, and D. Helbing, "Delays, inaccuracies and anticipation in microscopic traffic models," *Physica A*, vol. 360, no. 1, pp. 71–88, 2006.

[10] K. Zhou, J. C. Doyle, K. Glover, *et al.*, *Robust and optimal control.* Prentice hall New Jersey, 1996.

[11] K. Zhou and J. C. Doyle, *Essentials of robust control.* Prentice hall Upper Saddle River, NJ, 1998.

[12] S. Skogestad and I. Postlethwaite, *Multivariable feedback control: analysis and design.* Wiley New York, 2007.

[13] A. Weinmann, *Uncertain models and robust control.* Springer Science & Business Media, 2012.

[14] P. A. Ioannou and J. Sun, *Robust adaptive control.* Courier Corporation, 2012.

[15] K. S. Narendra and A. M. Annaswamy, *Stable adaptive systems.* Courier Corporation, 2012.

[16] E. Lavretsky and K. Wise, *Robust and adaptive control: with aerospace applications.* Springer Science & Business Media, 2012.

[17] K. J. Åström and B. Wittenmark, *Adaptive control.* Courier Corporation, 2013.

[18] T. Yucelen and W. M. Haddad, "A robust adaptive control architecture for disturbance rejection and uncertainty suppression with $\mathcal{L}_\infty$ transient and steady-state performance guarantees," *International Journal of Adaptive Control and Signal Processing*, vol. 26, no. 11, pp. 1024–1055, 2012.

[19] T. Yucelen, G. De La Torre, and E. N. Johnson, "Improving transient performance of adaptive control architectures using frequency-limited system error

dynamics," *International Journal of Control*, vol. 87, no. 11, pp. 2383–2397, 2014.

[20] H. P. Whitaker, J. Yamron, and A. Kezer, "Design of model reference control systems for aircraft," *Cambridge, MA: Instrumentation Laboratory, Massachusetts Institute of Technology*, 1958.

[21] P. V. Osburn, H. P. Whitaker, and A. Kezer, "New developments in the design of adaptive control systems," *Institute of Aeronautical Sciences*, 1961.

[22] A. Trujillo and I. Gregory, "Adaptive controller adaptation time and available control authority effects on piloting," *NASA Technical Reports Server*, 2013.

[23] A. C. Trujillo, I. M. Gregory, and L. E. Hempley, "Adaptive state predictor based human operator modeling on longitudinal and lateral control," in *AIAA Modeling and Simulation Technologies Conference*, p. 0654, 2015.

[24] D. H. Klyde and D. McRuer, "Smart-cue and smart-gain concepts development to alleviate loss of control," *Journal of guidance, control, and dynamics*, vol. 32, pp. 1409–1417, 2009.

[25] Y. Yildiz and I. Kolmanovsky, "Stability properties and cross-coupling performance of the control allocation scheme capio," *J. Guid. Contr. Dyn.*, vol. 34, no. 4, pp. 1190–1196, 2011.

[26] N. D. Richards, R. J. Adams, D. H. Klyde, and B. Cogan, "Flight-test evaluation of an adaptive controller for flying qualities specification and protection," *Journal of guidance, control, and dynamics*, vol. 38, pp. 2241–2256, 2015.

[27] M. Green, ""how long does it take to stop?" methodological analysis of driver perception-brake times," *Transportation Human Factors*, vol. 2, pp. 195–216, 2000.

[28] D. T. McRuer, "Mathematical models of human pilot behavior," Jan. 1974.

[29] N. Bekiaris-Liberis and M. Krstic, "Delay-adaptive feedback for linear feedforward systems,"

[30] R. Bellman and K. Cooke, *Differential-Difference Equations.* New York: Academic Press, 1963.

[31] G. Stépán, *Retarded Dynamical Systems: Stability and Characteristic Function.*

[32] R. Sipahi, S. i. Niculescu, C. T. Abdallah, W. Michiels, and K. Gu, "Stability and stabilization of systems with time delay," *IEEE Control Systems Magazine*, vol. 31, pp. 38–65, Feb 2011.

[33] M. Bando, K. Hasebe, K. Nakanishi, and A. Nakayama, "Analysis of optimal velocity model with explicit delay," *Physical Review E*, vol. 58, pp. 5429–5435, 1998.

[34] G. Niemeyer, C. Preusche, S. Stramigioli, and D. Lee, *Telerobotics*, pp. 1085–1108. Cham: Springer International Publishing, 2016.

[35] M. Ferre, M. Buss, R. Aracil, C. Melchiorri, and C. Balaguer, *Advances in Telerobotics.* Springer-Verlag Berlin Heidelberg, 2007.

[36] T. B. Sheridan, "Teleoperation, telerobotics and telepresence: a progress report," *Conrol Eng. Practice*, vol. 3, no. 2, pp. 205 – 214, 1995.

[37] T. Yucelen, Y. Yildiz, R. Sipahi, E. Yousefi, and N. Nguyen, "Stability limit of human-in-the-loop model reference adaptive control architectures," *International Journal of Control*, vol. 0, no. 0, pp. 1–18, 2017.

[38] K. Abidi, Y. Yildiz, and B. E. Korpe, "Explicit time-delay compensation in teleoperation: An adaptive control approach," *International journal of robust and nonlinear control*, vol. 26, pp. 3388 – 3403, 2016.

[39] D. B. Kaber, Y. Li, M. Clamann, and Y.-S. Lee, "Investigating human performance in a virtual reality haptic simulator as i nfluenced by fidelity and system latency," *IEEE transactions on systems, man, and cybernetics—part a: systems and humans*, vol. 42, no. 6, pp. 1562 – 1566, 2012.

[40] C. Smith and H. I. Christensen, "A minimum jerk predictor for teleoperation with variable time delay," in *International conference on inteligent robots and systems*, 2009.

[41] N. Hogan, “An organizing principle for a class of voluntary movements,” *The journal of neuroscience*, vol. 4, no. 11, pp. 2745 – 2754, 1984.

[42] D. Feth, A. Peer, and M. Buss, “Incorporating human haptic interaction models into teleoperation systems,” in *IEEE/RSJ international conference on intelligent robots and systems*, (Taipei, Taiwan), Oct. 2010.

[43] E. Slawiñski and V. Mut, “Pd-like controllers for delayed bilateral teleoperation of manipulators robots,” *International Journal of Robust and Nonlinear Control*, vol. 25, pp. 1801 – 1815, 2014.

[44] S. Li, L. Yang, Z. Gao, and K. Li, “Stabilization strategies of a general nonlinear car-following model with varying reaction-time delay of the drivers,” {*ISA*} *Transactions*, vol. 53, no. 6, pp. 1739 – 1745, 2014.

[45] D. M. Acosta, Y. Yildiz, R. W. Craun, S. D. Beard, M. W. Leonard, G. H. Hardy, and M. Weinstein, “Piloted evaluation of a control allocation technique to recover from pilot-induced oscillations,” *Journal of Aircraft*, vol. 52, no. 1, pp. 130–140, 2015.

[46] Y. Yildiz and I. Kolmanovsky, “Stability properties and cross-coupling performance of the control allocation scheme capio,” *Journal of Guidance, Control, and Dynamics*, vol. 34, no. 4, pp. 1190–1196, 2011.

[47] D. H. Klyde, D. T. McRuer, and T. T. Myers, “Pilot-induced oscillation analysis and prediction with actuator rate limiting,” *Journal of Guidance, Control, and Dynamics*, vol. 20, no. 1, pp. 81–89, 1997.

[48] A. Denasi, D. Kostic, and H. Nijmeijer, “Time delay compensation in bilateral teleoperations using impact,” *IEEE Transactions on Control Systems Technology*, vol. 21, no. 3, pp. 704 – 715, 2013.

[49] A. Takhmar, I. G. Polushin, A. Talasaz, and R. V. Patel, “Cooperative teleoperation with projection-based force reflection for mis,” *IEEE Transactions on Control Systems Technology*, vol. 23, no. 4, pp. 1411 – 1426, 2015.

[50] K. Hashtrudi-Zaad and S. E. Salcudean, "Analysis of control architectures for teleoperation systems with impedance/admittance master and slave manipulators," *The International Journal of Robotics Research*, vol. 20, no. 6, pp. 419 – 445, 2001.

[51] R. Sipahi and N. Olgac, "Complete stability robustness of third-order LTI multiple time-delay systems," *Automatica*, vol. 41, no. 8, pp. 1413 – 1422, 2005.

[52] R. Sipahi, *Cluster Treatment of Characteristic Roots, CTCR, A Unique Methodology for the Complete Stability Robustness Analysis of Linear Time Invariant Multiple Time Delay Systems against Delay Uncertainties.* PhD thesis, University of Connecticut, 2005.

[53] T. H. Massie and J. K. Salisbury, "The PHANToM haptic interface: A device for probing virtual objects," in *Proceedings of the ASME Dynamic Systems and Control Division*, pp. 295–301, 1994.

[54] Z. Najdovski and S. Nahavandi, *Extending Haptic Device Capability for 3D Virtual Grasping*, pp. 494–503. Berlin, Heidelberg: Springer Berlin Heidelberg, 2008.

[55] H. G. Teklemariam and A. K. Das, "A case study of phantom omni force feedback device for virtual product design," *International Journal on Interactive Design and Manufacturing (IJIDeM)*, vol. 11, pp. 881–892, Nov 2017.

[56] I. G. Polushin, A. Takhmar, and R. V. Patel, "Projection-based force-reflection algorithms with frequency separation for bilateral teleoperation," *IEEE/ASME Transactions on Mechatronics*, vol. 20, no. 1, pp. 143 – 154, 2015.

[57] D. Sun, F. Naghdy, and H. Du, "Time domain passivity control of time-delayed bilateral telerobotics with prescribed performance," *Nonlinear Dynamics*, vol. 87, no. 2, pp. 1253–1270, 2017.

[58] K. K. Karunakaran, K. M. Abbruzzese, H. Xu, and R. A. Foulds, "The importance of haptics in generating exoskeleton gait trajectory using alternate motor inputs," *IEEE Transactions on Neural Systems and Rehabilitation Engineering*, vol. 25, pp. 2328–2335, Dec 2017.

[59] M. C. Çavuşoğlu, D. Feygin, and F. Tendick, "A critical study of the mechanical and electrical properties of the PHANToM haptic interface and improvements for high performance control," *Presence: Teleoperators and Virtual Environments*, vol. 11, no. 6, pp. 555 – 568, 2002.

[60] A. M. Tahmasebi, B. Taati, F. Mobasser, and K. Hashtrudi-Zaad, "Dynamic parameter identification and analysis of a PHANToM haptic device," in *Proceedings of 2005 IEEE Conference on Control Applications, 2005. CCA 2005.*, pp. 1251–1256, Aug 2005.

[61] A. Nygaard, "High-level control system for remote controlled surgical robots," Master's thesis, Norwegian University of Science and Technology, Jun. 2008.

[62] A. J. Silva, O. A. D. Ramirez, V. P. Vega, and J. P. O. Oliver, "PHANToM OMNI haptic device: Kinematic and Manipulability," in *2009 Electronics, Robotics and Automotive Mechanics Conference (CERMA)*, pp. 193–198, Sep. 2009.

[63] B. Milne, C. Hann, and X. Chen, "The "α-invariant"": An energy-based nonlinear minimal damping model for robotic joints with friction," *ASME Journal of Computational and Nonlinear Dynamics*, vol. 12, pp. 041011–041011–10, Jan. 2017.

[64] F. L. Lewis, A. Yesildirek, and K. Liu, "Multilayer neural-net robot controller with guaranteed tracking performance," *IEEE Trans. Neural Networks*, vol. 7, pp. 388–399, 1996.

[65] F. L. Lewis, K. Liu, and A. Yesildirek, "Neural net robot controller with guaranteed tracking performance," *IEEE Trans. Neural Networks*, vol. 6, pp. 703–715, 1995.

[66] W. M. Haddad, V. Chellaboina, and N. A. Kablar, "Nonlinear impulsive dynamical systems Part I: Stability and dissipativity," in *Proc. IEEE Conf. Dec. Contr.*, (Phoenix, AZ), pp. 4404–4422, December 1999. Also in *Int. J. Contr.*, vol.74, pp.1631-1658, 2001.

[67] K. S. Narendra and A. M. Annaswamy, "A new adaptive law for robust adaptation without persistent excitation," *IEEE Trans. Autom. Control*, vol. 32, no. 2, pp. 134–145, 1987.

[68] P. Ioannou and P. Kokotovic, "Instability analysis and improvement of robustness of adaptive control," *Automatica*, vol. 20, no. 5, pp. 583–594, 1984.

[69] J. B. Pomet and L. Praly, "Adaptive nonlinear regulation: Estimation from Lyapunov equation," *IEEE Trans. on Autom. Ctrl.*, vol. 37, pp. 729–740, 1992.

[70] T. Yucelen and A. J. Calise, "Kalman filter modification in adaptive control," *Journal of Guidance, Control, and Dynamics*, vol. 33, no. 2, pp. 426–439, 2010.

[71] N. Nguyen, K. Krishnakumar, and J. Boskovic, "An optimal control modification to model-reference adaptive control for fast adaptation," *Proc. AIAA Guid., Navig., and Contr. Conf.*, Honolulu, Hawaii, 2008.

[72] N. Nguyen, M. Bakhtiari-Nejad, and A. Ishihira, "Robust adaptive optimal control with large adaptive gain," *Proc. Amer. Contr. Conf.*, St. Louis, MO, 2010.

[73] T. Yucelen, A. J. Calise, and N. T. Nguyen, "Evaluation of derivative-free adaptive controller with optimal control modification," in *Proceedings of the 2011 AIAA Guidance, Navigation, and Control Conference. Portland, Oregon*, 2011.

[74] A. J. Calise and T. Yucelen, "Adaptive loop transfer recovery," *Journal of Guidance, Control, and Dynamics*, vol. 35, no. 3, pp. 807–815, 2012.

[75] G. Chowdhary and E. N. Johnson, "Theory and flight test validation of a concurrent learning adaptive controller," *AIAA J. Guid. Contr. Dyn.*, vol. 34, pp. 592–607, 2010.

[76] G. Chowdhary, T. Yucelen, M. Mühlegg, and E. N. Johnson, "Concurrent learning adaptive control of linear systems with exponentially convergent bounds," *International Journal of Adaptive Control and Signal Processing*, vol. 27, no. 4, pp. 280–301, 2013.

[77] T. Yucelen and A. J. Calise, "Derivative-free model reference adaptive control," *Journal of Guidance, Control, and Dynamics*, vol. 34, no. 4, pp. 933–950, 2011.

[78] T. Yucelen and W. M. Haddad, "Low-frequency learning and fast adaptation in model reference adaptive control," *Automatic Control, IEEE Transactions on*, vol. 58, no. 4, pp. 1080–1085, 2013.

[79] T. Yucelen, B. Gruenwald, and J. A. Muse, "A direct uncertainty minimization framework in model reference adaptive control," in *AIAA Guidance, Navigation, and Control Conference*, 2015.

[80] B. Gruenwald and T. Yucelen, "On transient performance improvement of adaptive control architectures," *International Journal of Control*, vol. 88, no. 11, pp. 2305–2315, 2015.

[81] H. K. Khalil, *Nonlinear Systems.* Upper Saddle River, NJ: Prentice Hall, 1996.

[82] D. Breda, S. Maset, and R. Vermiglio, "Pseudospectral differencing methods for characteristic roots of delay differential equations," *SIAM Journal of Scientific Computing*, vol. 27, pp. 482–495, 2006.

[83] K. Engelborghs, T. Luzyanina, and D. Roose, "Numerical Bifurcation Analysis of Delay Differential Equations Using DDE-BIFTOOL," *ACM Transactions on Mathematical Software*, vol. 1, no. 1, pp. 1–21, 2000.

[84] T. Vyhlidal and P. Zitek, "Mapping based algorithm for large-scale computation of quasi-polynomial zeros,"

[85] S. Yi, P. W. Nelson, and A. G. Ulsoy, *Time-delay Systems: Analysis and Control Using the Lambert W Function.* World Scientific Publishing Company, 2010.

[86] A. E. Bryson, *Control of Spacecraft and Aircraft.* Princeton University Press, 1994.

[87] D. McRuer, "Human dynamics and pilot-induced oscillations," *Minta Martin Lecture*, 1992. Massachusetts Institute of Technology, Cambridge, MA.

[88] K. Ogata, *Modern Control Engineering.* Upper Saddle River, NJ: Pearson, 5 ed., 2010.

[89] R. Eflese, "Simulated annealing: a tool for operational research," *European Journal of Operational Research*, 1990.

[90] S. Kirkpatrick, C. D. Gelatt, and M. P. Vecchi, "Optimization by simulated annealing," *Science, New Series*, 1983.

[91] N. Metrolpolis, A. Rosenbluth, M. Rosenbluth, A. H. Teller, and E. Teller, "Equations of state calculations by fast computing machines," *The Journal of Chemical Physics*, 1953.

[92] Z. V. Rekasius, "A stability test for systems with delays," in *Joint Automatic Control Conference*, 1980.

[93] R. R. Hendrix, *Robotically assisted eye surgery: a haptic master console.* PhD thesis, Technische Universiteit Eindhoven, 2011.

[94] D. Thorby, "13 - vibration testing," in *Structural Dynamics and Vibration in Practice* (D. Thorby, ed.), pp. 367 – 385, Oxford: Butterworth-Heinemann, 2008.